Analysis and Characterization of an Unclassified RFI Affecting Ionospheric Amplitude Scintillation Index Over the Mediterranean Area

Emanuele Pica, Alex Minetto, *Member, IEEE*, Claudio Cesaroni, and Fabio Dovis, *Member, IEEE*

***Abstract*—Radio frequency (RF) signals transmitted by Global Navigation Satellite Systems (GNSSs) are exploited as signals of opportunity in many scientific activities, ranging from sensing waterways and humidity of the terrain to the monitoring of the ionosphere. The latter can be pursued by processing the GNSS signals through dedicated ground-based monitoring equipment, such as the GNSS Ionospheric Scintillation and Total Electron Content Monitoring (GISTM) receivers. Nonetheless, GNSS signals are susceptible to intentional or unintentional RF interferences (RFIs), which may alter the calculation of the scintillation indices, thus compromising the quality of the scientific data and the reliability of the derived space weather monitoring products. Upon the observation of anomalous scintillation indices computed by a GISTM receiver in the Mediterranean area, the study presents the results of the analysis and characterization of a deliberate, unclassified interferer acting on the L1/E1 GNSS signal bands, observed and captured through an experimental, software-defined radio setup. This article also highlights the adverse impacts of the interferer on the amplitude scintillation indices employed in scientific investigations, and presents a methodology to discriminate among regular and corrupted scintillation data. To support further investigations, a dataset of baseband signals samples affected by the RFI is available at IEEE DataPort.**

***Index Terms*—Global Navigation Satellite Systems (GNSSs), ionospheric monitoring, ionospheric scintillations, radio frequency interferences (RFIs), remote sensing.**

I. Introduction

GLOBAL Navigation Satellite System (GNSS) signals crossing small-scale electron density irregularities in the ionosphere may be subject to rapid fluctuations of their amplitude and phase known as ionospheric scintillations. This is due to the diffractive effects induced on the signals by ionospheric irregularities smaller than the Frasnel scale (few hundred meters for the L-band) [1], [2], [3], [4], [5]. Ionospheric scintillations may cause cycle slips and loss of lock of the GNSS signals, thus hindering the accuracy and integrity of precise positioning applications [6], [7], [8]. Ionospheric irregularities inducing scintillations on L-band signals are due to different causes depending on the latitude. In particular, at high latitude, scintillations are mainly caused by the solar wind–magnetosphere–ionosphere coupling (see, e.g., [9]), while at low latitude (where they are more likely to occur) are mainly due to the formation of small-scale irregularities embedded in the equatorial plasma bubbles (EPB) (see, e.g., [10], [11], [12], [13], and [14]). At mid latitude, ionospheric scintillations can be due to poleward expansion of the crests of the equatorial ionization anomaly (EIA) [15] or equatorward expansion of the auroral oval during geomagnetic storms [16]. Very few cases of mid latitude GNSS scintillations during quiet times are reported in the literature [17]. By exploiting the GNSS signals transmitted by medium-Earth orbit (MEO) and geostationary-Earth orbit (GEO) satellites as signals-of-opportunity, it is possible to investigate the ionospheric irregularities for scientific purposes, as well as to monitor ionospheric scintillations in the framework of operational space weather services [18]. This is achieved by means of ground-based passive instruments, such as the GNSS ionospheric scintillation and total electron content monitor (GISTM) receivers [19], which provide the estimation of the so-called amplitude and phase scintillation indices (S_4 and σ_ϕ, respectively), allowing to quantify ionospheric scintillations [20]. Besides ionospheric irregularities, however, a number of different phenomena related to both space weather events (e.g., solar radio burst [21], [22]) and environmental conditions may impair the GNSS signals and the detection of ionospheric scintillations. A well-recognized source of error in the computation of the scintillation indices is the reception of GNSS signals from multiple paths due to the reflections caused by obstacles in the proximity of the receiving antenna, known as multipath [23]. To compensate for such phenomena, GISTM receiver antennas are typically deployed in multipath-free conditions, i.e., isolated areas with limited natural or anthropogenic obstacles, and elevation masks can be configured to neglect multipath-susceptible signals received from low-elevation satellites [24].

Similarly to the errors induced by the multipath, misleading effects on navigation signals (and on the scintillation indices

Manuscript received 10 January 2023; revised 10 March 2023, 5 April 2023, and 6 April 2023; accepted 8 April 2023. Date of publication 13 April 2023; date of current version 14 September 2023. This work was supported by INGV through research project "Pianeta Dinamico, Theme 8 - ATTEMPT" under Grant C.U.P. D53J19000170001, founded by the Italian Ministry of University and Research ("Fund aimed at relaunching the investments of central administrations of the state and the development of the country", act 145/2018). The work of Alex Minetto was supported by the Programma Operativo Nazionale (PON) Ricerca ed Innovazione of the Italian Ministry of University and Research (MUR) through research contract under Grant 32-G-13427-5 DM 1062/2021. *(Corresponding authors: Emanuele Pica; Alex Minetto; Claudio Cesaroni; Fabio Dovis.)*

Emanuele Pica and Claudio Cesaroni are with the Environment Department of the Istituto Nazionale di Geofisica e Vulcanologia (INGV), 00143 Rome, Italy (e-mail: emanuele.pica@ingv.it; claudio.cesaroni@ingv.it).

Alex Minetto and Fabio Dovis are with the Department of Electronics and Telecommunications (DET), Politecnico di Torino, 10129 Turin, Italy (e-mail: alex.minetto@polito.it; fabio.dovis@polito.it).

Digital Object Identifier 10.1109/JSTARS.2023.3267003

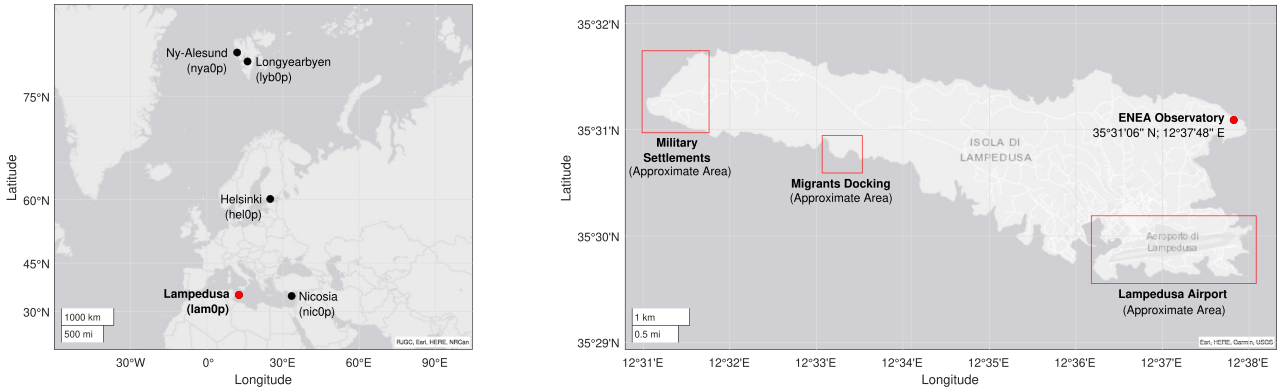

Fig. 1. (a) INGV ionospheric scintillation monitoring network in the European area and (b) detail of Lampedusa island (Italy) showing the position of the ENEA observatory and other areas of interest.

derived from them) can also be observed due to intentional or unintentional in-band Radio Frequency Interferences (RFIs) captured by the instrument receiving antenna [23], [25], [26], [27]. These interferences are typically attributed to malicious actions aiming at disrupting GNSS receivers' operational activities by forcing misleading position, velocity, and timing (PVT) estimation, degrading their estimation accuracy up to cause a denial of their positioning, navigation, and timing (PNT) capabilities (a.k.a. denial-of-service attack) [28]. These attacks are classified as spoofing, meaconing, and jamming, with the first aiming at fooling receivers' operations by transmitting plausible yet fake GNSS signals, and the latter aiming at transmitting structured or unstructured radio frequency (RF) signals to disturb or blind the receiver's RF chain. Despite a lack of literature, alternative yet unauthorized misuse of the GNSS bands may be also referred to as RF steganography [29], [30], aiming at hiding data transmission in unsuspected portions of the RF spectrum. Such undocumented actions may turn into GNSS jamming when the received RFI power is at least comparable to the received power of legitimate GNSS signals. Despite the effects of RFIs on the PNT performance of GNSS receivers can be quantified through systematic analysis [31], the impact of RFIs on the computation of the scintillation indices has been only demonstrated through a controlled simulation environment in few pioneering studies [25], [26]. In order to detect RFIs in real scenarios, intermediate frequency (IF) or baseband samples of GNSS signals can be recorded and analyzed by emulating the processing chain of a conventional GNSS receiver through highly flexible software-defined radio (SDR) framework [32], [33]. To this aim, the use of SDR equipment has been demonstrated as a powerful tool to support the analysis of GNSS signals recorded at remote locations [34], [35]. Further examples of RFI detection strategies are extensively documented in satellite-based remote sensing applications that leverage similar approaches [36], [37], [38], [39].

In this article, we present the investigation carried out by the Istituto Nazionale di Geofisica e Vulcanologia (INGV) and the Department of Electronics and Telecommunications (DET) of Politecnico di Torino to assess the nature of several anomalies observed in the S_4 index computed by a GISTM receiver operating in Lampedusa island (35°31'06" N; 12°37'48" E), Italy. The observatory is part of the INGV ionospheric monitoring network [40] shown in Fig. 1(a) and is hosted at the Climate Observation Station of the Italian National Agency for New Technologies, Energy and Sustainable Economic Development (ENEA), visible in Fig. 1(b). At the mid-latitudes monitored by the receiver, the aforementioned anomalies were observed for the first time during summer 2020, but similar seasonal repetition and daily patterns appears again during 2021. Unlike low-latitudes, ionospheric scintillations in the Mediterranean sector do not show any seasonal or daily regular patterns and are due, as already pointed-out, to disturbed geomagnetic conditions. Moreover, the political and environmental situation of Lampedusa may favor deliberate RF transmissions against navigation and communication systems: the island hosts military settlements and NATO radar equipment, a civilian and military airport, and is a hotspot of irregular migratory flows from the coast of North Africa [41], [42]. Furthermore, possible RFIs in the area were detected in the second semester of 2020 by Airbus aircrafts [43], and a recent paper has highlighted intense RFIs in the Mediterranean region by analyzing the data of the GNSS receivers carried by GRACE Follow-On (GRACE-FO) low Earth orbit (LEO) satellites [44].

Moving from the know-how gathered during previous, joint test campaigns and activities [34], [45], [46], a renewed, SDR-based hardware and software architecture was designed and implemented to perform long-term grabbing of GNSS RF signal samples in the attempt to identify and characterize the source of the disturbances.

The main contributions of this article are the following.

1) We prove the presence of an interferer affecting the GNSS signal in the Lampedusa area and present a characterization of the RFI through the analysis of the IF samples acquired by the dedicated SDR architecture. We discuss the impact of such interference on the estimation of the amplitude scintillation index and propose an analytic model of the interferer, which may allow for further theoretical analyses and the development of mitigation techniques.
2) We assess the adverse impact of the RFIs on the scintillation data computed through the GISTM receiver, which may impair both near real-time monitoring applications

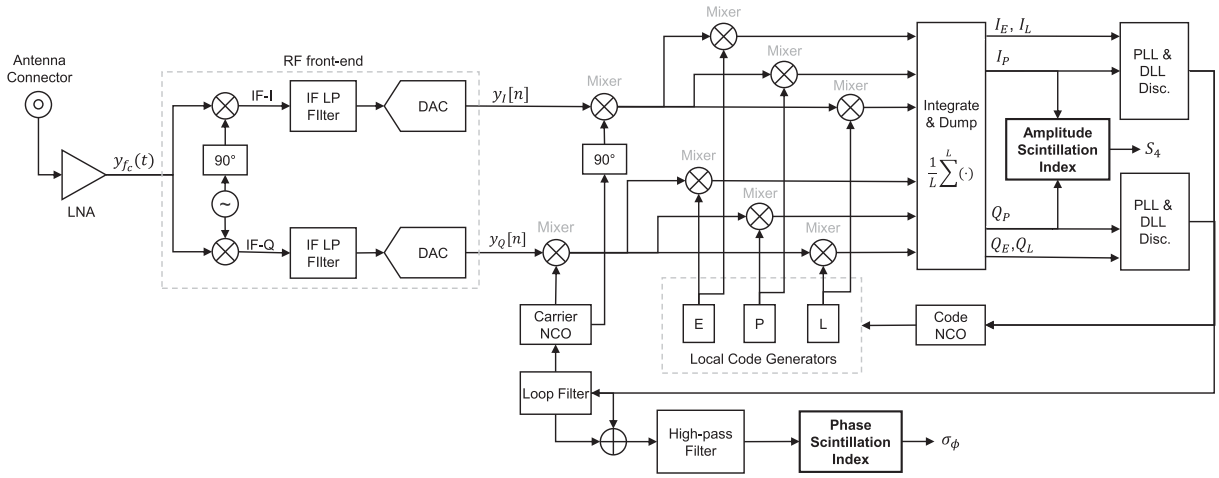

Fig. 2. Block diagram of a conventional, single-channel tracking loop architecture for GNSS receivers. I_p and Q_p outputs from the prompt correlator (P) are employed in the estimation of amplitude scintillation indices, i.e., S_4, while σ_ϕ is estimated through the output of the loop filter in charge of tracking the IF or the residual carrier frequency.

as well as scientific investigations of ionospheric scintillation. At the time of writing, on-field proofs of such a vulnerability are still undocumented in the literature. We also propose a preliminary methodology to automatically detect and filter the interfered observation from the collected data.

The rest of this article is organized as follows. Section II provides background information about the computation of scintillation indices through GNSS signals in GISTM receivers. Section III presents a preliminary analysis of the anomalies detected in the scintillation data generated by the GISTM receiver, with the aim to eventually exclude real scintillation phenomena induced by the ionosphere as the cause of the observed anomalies. Section IV describes the experimental SDR setup deployed at the monitoring station and presents the analysis tools exploited for the investigation and characterization of the interferer as well as for the detection and filtering of the anomalies from the scintillation data. Section V reports the results of the aforementioned analysis, while a discussion about the results and hypothesis about the nature of the disturbances is given in Section VI. Finally, Section VII concludes this article and presents further works.

II. Background

A. GNSS Signal and Receiver Models

To provide ionospheric scintillation indices, a GNSS receiver must receive GNSS signals from Line-of-Sight (LOS) satellites and track their numerical counterparts. Signals from multiple satellites are managed in a multichannel architecture, and the associated indices are independently provided for each channel. According to the scheme of Fig. 2, the received signal at the input of the receiver's front-end is modeled as

$$y_{f_c}(t) = x_{\text{GNSS},f_c}(t) + x_{\text{RFI}}(t) + w_{\text{RX}}(t) \tag{1}$$

where x_{GNSS,f_c} is the sum of the received GNSS signals from the visible satellites at the receiver location for a given bandwidth and center frequency f_c [47], and x_{RFI} identifies any possible incoherent, in-band RFI [28]. Both useful and interfering signal components in (1) account for nonidealities due to the respective RF propagation channels. Eventually, w_{RX} models the additive thermal noise introduced by the receiving chain and the quantization noise injected by the analog-to-digital conversion (ADC) operated at the RF front-end. Within this study, GNSS signals are considered continuously available at the receiver while RFI terms may occasionally occur. The RF front-end downconverts the input signal to a predefined IF prior to its sampling and quantization at the ADC. As shown in Fig. 2, the baseband numerical samples from in-phase (I) and quadrature (Q) branches are correlated with early (E), prompt (L), and late (L) replicas of the locally generated spreading code. Eventually, the integrate and dump block provides prompt in-phase (I_p) and quadrature (Q_p) samples, which are used to estimate the S_4 index, while the σ_ϕ index is derived through the output of the loop filter in charge of tracking the IF carrier, as depicted by the bottom branch of the diagram in Fig. 2.

B. Amplitude and Phase Scintillation Indices

The S_4 and σ_ϕ are the statistical indices typically adopted to quantify ionospheric scintillations based upon received GNSS signals features. S_4 measures the variability of the signal intensity (SI), that is estimated as

$$\text{SI} = \text{WBP} - \text{NBP} \tag{2}$$

where wide-band power (WBP) and narrow-band power (NBP) are, respectively, defined as

$$\text{WBP} = \sum_{i=0}^{M} \left(I_i^2 + Q_i^2\right) \tag{3}$$

and

$$\text{NBP} = \left(\sum_{i=0}^{M} I_i\right)^2 + \left(\sum_{i=0}^{M} Q_i\right)^2 \tag{4}$$

and the I and Q terms in (3) and (4) are the I_p and Q_p components of the received signal after the integrate and dump operation performed by the receiver tracking stage, and M is the total number of accumulated periods. The S_4 index is defined as the normalized standard deviation of the detrended 50-Hz raw signal intensity over a given interval of time, typically 60 s

$$S_4' = \sqrt{\frac{\langle \mathrm{SI}^2 \rangle - \langle \mathrm{SI} \rangle^2}{\langle \mathrm{SI} \rangle^2}} \tag{5}$$

where $\langle \cdot \rangle$ is the time average operator over the observation window. The contribution of the noise to the overall value of S_4 can be estimated as

$$S_{4,n} = \sqrt{\frac{\alpha}{\langle C/N_0 \rangle} \left(1 + \frac{\beta}{\gamma \, \langle C/N_0 \rangle} \right)} \tag{6}$$

where C/N_0 is the estimated carrier-to-noise ratio [48], and $\alpha = 100$, $\beta = 500$, and $\gamma = 19$, as proposed in [20]. Equation (6) provides an estimate of the noise standard deviation over the target time span (i.e., 60 s) and is typically obtained through the signal component, I or Q, carrying a nearly orthogonal spreading code that does not correlate with the code of interest, thus returning a noise-like behavior. Eventually, a refined estimate of S_4 can be computed by removing the noise contribution, as

$$S_4 = \sqrt{(S_4')^2 - S_{4,n}^2}. \tag{7}$$

The estimation of S_4 through (7) may be affected by unexpected variation of the C/N_0 unrelated to ionospheric irregularities, such as in the presence of RFIs producing misleading values of the index, thus triggering false evaluation of amplitude ionospheric scintillation. The σ_ϕ index is defined as the standard deviation of the 50-Hz detrended carrier phase over a given interval of time, typically 60 s and is given in radians, as

$$\sigma_\phi = \sqrt{\langle \Phi^2 \rangle - \langle \Phi \rangle^2}. \tag{8}$$

The σ_ϕ seems not affected by the events investigated in this study, but it will be recalled for the sake of completeness in Section III for an exhaustive analysis of the anomalous scintillation events. The scintillation indices are calculated along the line-of-sight (slant S_4 and σ_ϕ) of the GNSS signals transmitted by those satellites in the receiver's field of view (FoV), and filters with a fixed cutoff frequency of 0.1 Hz are usually adopted for data detrending. The detection of ionospheric scintillations can be performed by comparing the aforementioned indices against predefined thresholds, allowing a preliminary classification of the severity of the events; typical thresholds and associated events intensity are reported in Table I.

TABLE I
CONVENTIONAL THRESHOLDS FOR THE CLASSIFICATION OF IONOSPHERIC SCINTILLATION EVENTS BASED UPON AMPLITUDE AND PHASE INDICES [49]

Index	Event Intensity	Threshold
S_4	Quiet	$S_4 \leq 0.1$
	Weak	$0.1 < S_4 \leq 0.25$
	Moderate	$0.25 < S_4 \leq 0.7$
	Severe	$S_4 > 0.7$
σ_ϕ (rad)	Quiet	$\sigma_\phi \leq 0.1$
	Weak	$0.1 < \sigma_\phi \leq 0.25$
	Moderate	$0.25 < \sigma_\phi \leq 0.7$
	Severe	$\sigma_\phi > 0.7$

III. PRELIMINARY ANALYSIS

A. Lampedusa GISTM Station

The ionospheric observatory of Lampedusa hosts, since 2018, a Septentrio PolaRx5S GISTM receiver. The PolaRx5S is a multifrequency, multiconstellation GNSS receiver equipped with a low-noise oven-controlled crystal (Xtal) oscillator. It acquires, for every satellite in view and for every available frequency, the raw phase (in cycles) and postcorrelation I_p and Q_p samples with a sampling rate of 50 Hz, as per the generalized architecture presented in Section II-A. It is able to provide, with a 1-min resolution, the S_4 and σ_ϕ indices together with the total electron content (TEC) and its rate of change (ROT). The data acquired by the station are transmitted in near-real time to the INGV Space Weather Information Technology system and collected into a database publicly accessible to the scientific community through the electronic Space Weather upper atmosphere (eSWua[1]) website [50]. These data are also provided to the PECASUS consortium[2] for the provision of Space Weather services to the International Civil Aviation Organization [18].

B. Investigation About the S_4 Anomalies

The following analysis focuses on the scintillation indices recorded by the GISTM receiver during August 2021 wherein several anomalies were observed in the collected data. In order to avoid misleading contributions possibly caused by multipath effects, only satellites with elevation above 30° are considered; indeed, the Lampedusa observatory is located nearby a lighthouse, whose building was proven as a nonnegligible source of multipath for those signals acquired at lower elevations, as it will be shown in the results of Section V-C. The area observed by the receiver, considering this elevation mask, covers the mid-latitudes between 30°N and 40°N and a longitudinal sector between 7°E and 19°E. The signals taken into consideration are the one belonging to the Global Positioning System (GPS), Galileo, BeiDou Navigation Satellite System (BDS), and GLONASS constellations. The reported S_4 and σ_ϕ indices are the slant values calculated at 1-min resolution from the L1/E1 frequency band for each satellites in view in the considered time span.

Fig. 3(a) and (b) reports the maximum hourly values of the S_4 and σ_ϕ, respectively, recorded during August 2021. As it is possible to see from Fig. 3(a), several occurrences of the S_4 above the threshold of moderate scintillation [lower dotted red line in Fig. 3(a) and (b)] recurred during the month; the same behavior was not registered for the σ_ϕ [see Fig. 3(b)].

[1][Online]. Available: eswua.ingv.it
[2][Online]. Available: www.pecasus.eu

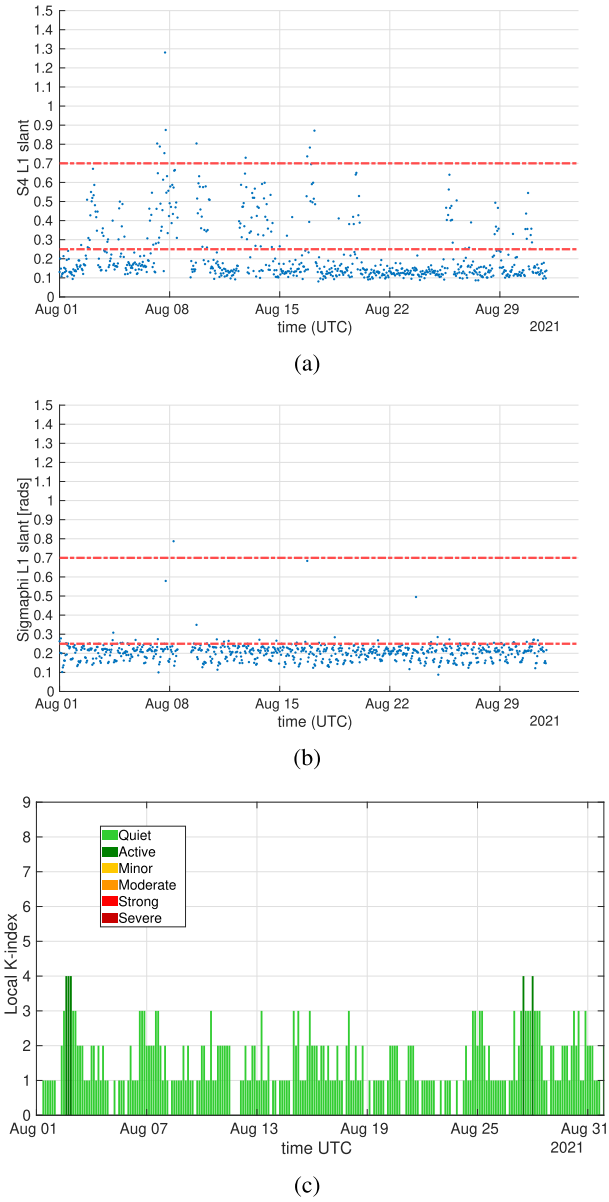

Fig. 3. Maximum hourly values of the (a) S_4 and (b) σ_ϕ during August 2021 (satellites elevation above 30°), and (c) local K-index recorded during the same period. Thresholds (dashed horizontal lines) of (a) and (b) are defined according to Table I.

The observed values of the S_4 are definitely unexpected considering 1) the latitudes covered by this analysis and 2) the overall space weather conditions registered during the month of August 2021. Indeed, as mentioned in Section I, ionospheric scintillation at the Mediterranean latitudes are not common and are generally caused by disturbed space weather conditions [15], [16], [51], [52] originating the so-called super fountain effect [53]. However, as Fig. 3(c) shows, no relevant geomagnetic storms capable to induce a poleward expansion of the crests of the EIA were detected during August 2021 according to the local K-index recorded at the INGV geomagnetic observatory of Lampedusa [54], [55]. It is worth recalling that the K-index quantifies the disturbances in the horizontal component of the magnetic field with respect to the quite conditions and can be employed as an indicator of the intensity of geomagnetic storms measured at a given geomagnetic observatory [56]. Usually, K-index values below 4 are representative of quiet/low-disturbed conditions, while values from 5 to 9 indicate minor to extreme storm conditions, respectively. Moreover, the diffractive effects induced by ionospheric irregularities on the GNSS signals passing through them will produce fluctuations of both the phase and amplitude of the signals, thus increasing the value of both the S_4 and σ_ϕ indices [5], [57], contrary to what shown by Fig. 3(a) and (b).

Further considerations on the observed temporal and spatial distributions of the scintillation indices, when compared with the case of a real ionospheric scintillation event, allow to eventually exclude ionospheric phenomena as the source of the observed anomalies. The following analysis focuses on the data of 7 August, 2021, when several anomalies were recorded, compared with the data of 10 March, 2022, when a real ionospheric scintillation event was detected over the area under investigation. With regards to the data of 7 August, 2021, Fig. 4(a) reports a daily view of the time profiles of the S_4 index, where different colors are attributed to the different satellites in view (space vehicle ID are reported in the legend). As Fig. 4(a) shows, the occurrences above the threshold of moderate scintillation seems to affect the signals from the majority of the satellites in view during the day; on the contrary, the time profile of the σ_ϕ does not exhibit similar patterns, as shown by Fig. 4(b). Fig. 4(c) reports a daily view of the maximum (blue line) and mean (green line) values of the S_4 index calculated on all the signals in view. As Fig. 4(c) suggests, most of the satellites in the FoV exhibit similar patterns; as a consequence, the S_4 mean and maximum values appear to be very close each other. Fig. 4(d) shows a daily view of the time profiles of the maximum S_4 values calculated among all the signals pertaining the same satellites constellation. From Fig. 4(d), it is possible to spot similar patterns among the GPS (blue line), Galileo (red line), and BDS (yellow line) satellites, while GLONASS satellites (purple line) seem to be not affected by scintillations most of the time. Finally, Fig. 6(a) reports on a geographic map the S_4 occurrences above the threshold of moderate scintillation ($S_4 > 0.25$) during the same day (7 August). The points on the map represent the ionospheric pierce points (IPP)s at 350 km for all the satellites in view and their color represents the values of the S_4. As Fig. 6(a) shows, moderate to severe scintillations are visible across the entire FoV of the receiver, while ionospheric scintillations in quiet geomagnetic conditions are more likely to occur in the proximity of the EIA crests, respectively, at ca. $\pm 20°$ from the magnetic equator. Similar features of the spatial and temporal distributions of the scintillation indices reported for 7 August were eventually observed in each day of August 2021 affected by the anomalies.

When comparing the previous temporal and spatial distributions of the indices with those recorded during the event of 10th of 10 March, 2022, it is possible to observe the expected behavior in the case of a real ionospheric scintillation event [see Fig. 5 and Fig. 6(b)] and eventually conclude that the anomalies were not induced by natural ionospheric phenomena. Indeed, given the small scale (a few hundreds of meters) of the irregularities leading to L-band scintillations, and considering the latitudes

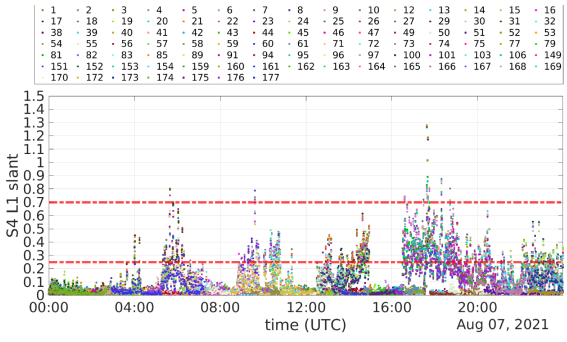

(a)

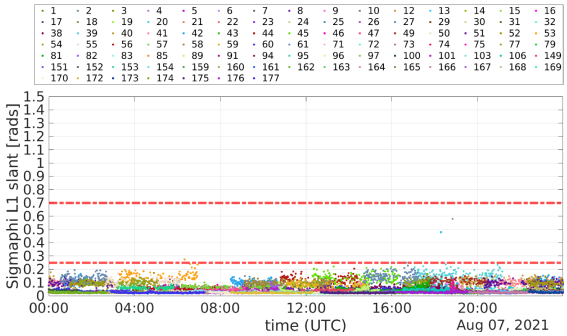

(b)

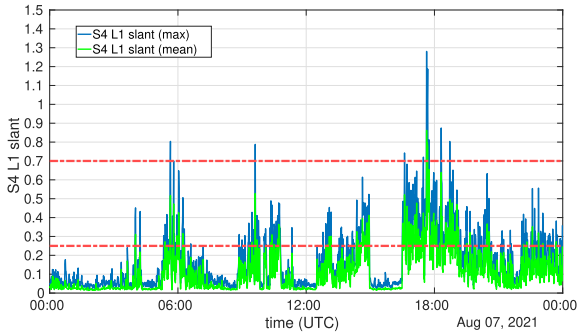

(c)

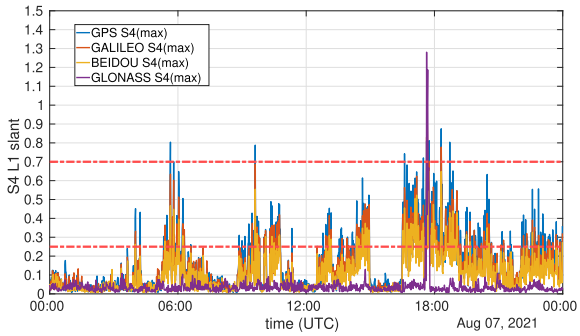

(d)

Fig. 4. (7 August, 2021) Scintillation indices affected by RFI. Thresholds (dashed horizontal lines) are defined according to Table I. (a) Time profile of the S_4. Different colors are attributed to the different satellites in view (space vehicle ID in the legend). (b) Time profile of the σ_ϕ. Different colors are attributed to the different satellites in view (space vehicle ID in the legend). (c) Time profile of the S_4 by considering maximum and mean values among all the available satellites. (d) Time profile of the S_4 by considering the maximum values among all the satellites pertaining the same GNSS constellation.

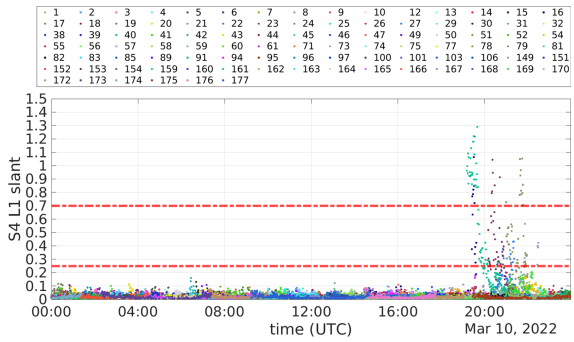

(a)

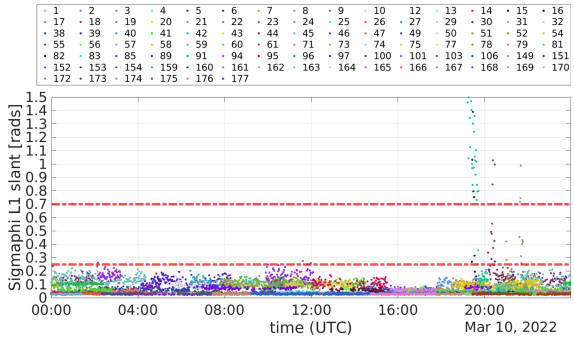

(b)

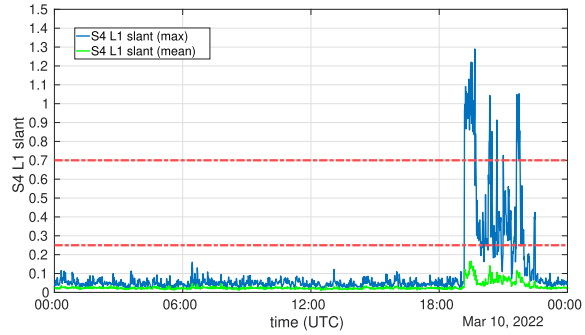

(c)

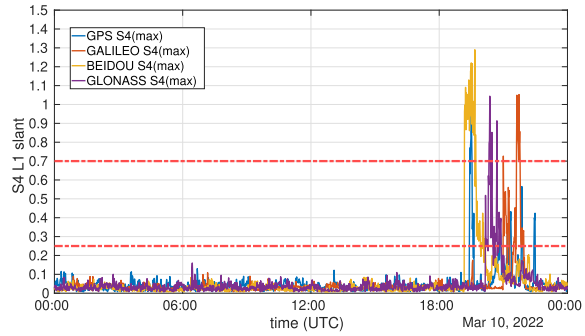

(d)

Fig. 5. (10 March, 2022) Scintillation indices in the case of real ionospheric scintillation event. Thresholds (dashed horizontal lines) are defined according to Table I. (a) Time profile of the S_4. Different colors are attributed to the different satellites in view (space vehicle ID in the legend). (b) Time profile of the σ_ϕ. Different colors are attributed to the different satellites in view (space vehicle ID in the legend). (c) Time profile of the S_4 by considering maximum and mean values among all the available satellites. (d) Time profile of the S_4 by considering the maximum values among all the satellites pertaining the same GNSS constellation.

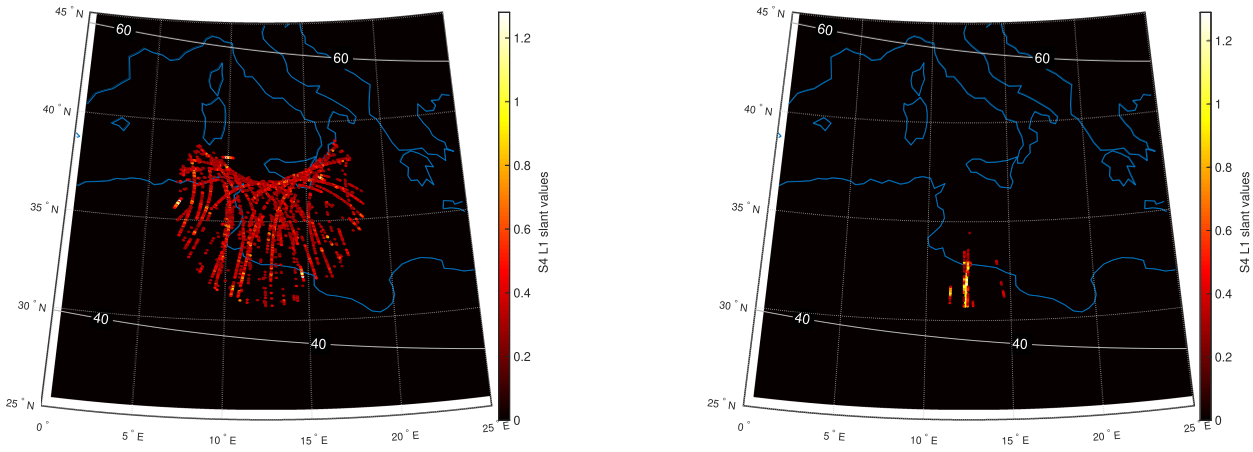

(a) (b)

Fig. 6. Map of the S_4 occurrences above the threshold of moderate scintillation ($S_4 > 0.25$) for (a) 7 August, 2021, and for (b) 10 March, 2022, and for satellites elevation above 30°. Geographic coordinates are labeled at the border of the maps and represented by the dotted lines inside the map; geomagnetic latitudes are labeled inside the maps and represented with the continuous lines.

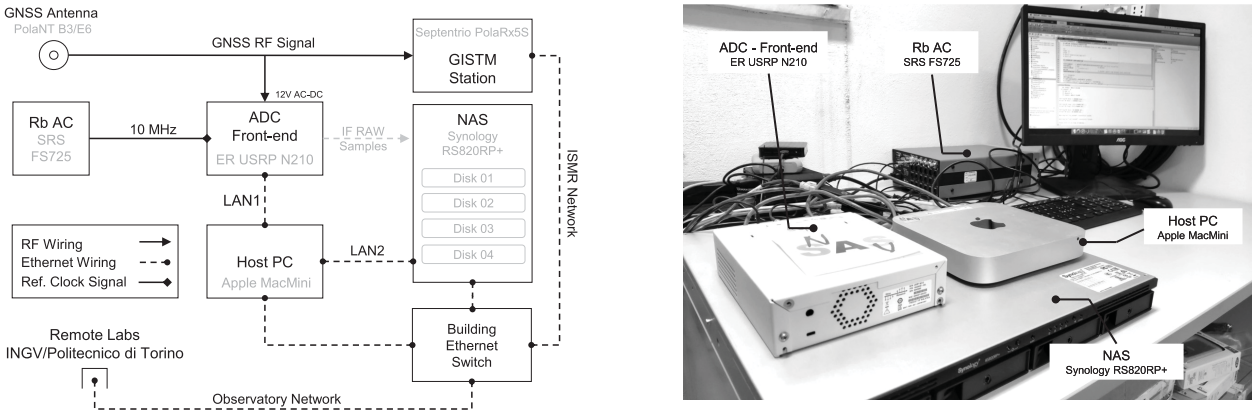

(a) (b)

Fig. 7. (a) Operational GISTM/SDR architecture for the grabbing of GNSS IF signal samples, and (b) actual deployment of the GISTM/SDR setup along with complementary equipment at the ENEA Station for Climate Observations in Lampedusa.

under investigation, not all the satellites in the FoV of the receiver are expected to be affected by scintillations; as a consequence, the mean and maximum values of the S_4 will exhibit different patterns, as shown by Fig. 5(c) [contrary to Fig. 4(c), when the RFI was present], and only localized area will result affected by scintillation, as shown by Fig. 6(b) [contrary to what is shown by Fig. 6(a)]. Moreover, ionospheric irregularities will impact the signals of any GNSS constellation passing through them, as shown by Fig. 5(d) [in comparison to Fig. 4(d)], and will induce scintillation on both amplitude and phase of the signals, as shown by Fig. 5(a) and (b) [in comparison to Fig. 4(a) and (b), respectively].

IV. Methodology

A. Experimental Setup and Data Collection

In September 2021, new investigations were carried out to assess the nature of the anomalies presented in Section III. In order to acquire possibly interfered GNSS signals, a dedicated experimental setup was deployed alongside the GISTM receiver, based on a SDR architecture. A high-level block scheme of the setup is provided in Fig. 7(a) while a picture of the operational hardware deployment is shown in Fig. 7(b). General-purpose SDR front-ends are typically employed for research and development activities in radio-communication systems as they facilitate the acquisition of RF signals through configurable and flexible hardware and software architectures. By exploiting such flexibility, the setup aims at collecting IF signals samples of the received GNSS L1-band (center frequency 1575.42 MHz) to perform investigations on possible intentional or unintentional interferences affecting the GNSS signals (and the derived scientific data) recorded on the island. At the time of writing, the experimental setup consists of an Ettus Research Universal Software Radio Peripheral (USRP) N210 front-end performing the ADC conversion of the input signal, and the grabbing of IF signal samples; an Apple MacMini PC, i.e., the host PC, that runs the signal acquisition routine; a Stanford Research Systems (SRS) Rubidium (Rb) atomic clock (AC) FS725 to provide

TABLE II
CONFIGURATION PARAMETERS OF THE FRONT-END AND THE ACQUISITION SOFTWARE

Symbol	Definition	Value
f_0	Center frequency	1575.42 MHz (L1)
f_{IF}	Intermediate frequency	0.00 MHz (baseband)
f_s	Sampling frequency	5 Msps
b_d	Bit depth	16 b (8I+8Q)
ΔT	acquisition interval	600 s (10 min)
T_{S_4}	S_4 Threshold	0.3

stable and reliable 10 MHz reference signal to the ER USRP, and a network-attached storage (NAS) for the storage of large data volume. A two-way splitter is exploited to feed both the GISTM receiver and the front-end with the RF signals received at the GNSS PolaNt Choke Ring B3/E6 antenna. The acquisition routine, continuously executed on the host PC, is being a part of a proprietary GNSS fully software receiver designed to emulate the processing chain of commercial receivers in a more flexible and controllable environment. The configuration parameters of the front-end and of the aforementioned acquisition routine are reported in Table II. To partially overcome the well-known issue of storing TBs of binary files produced by such systems, the Lampedusa setup took advantage of a NAS unit that directly stores the IF signal samples during the acquisition. Moreover, a fully automated procedure continuously acquires 24/7 the IF samples and daily freed the space on the NAS from the nonuseful datasets.

The first collection campaign provides 171 datasets of 10 min each (28.5 h), affected by the RFI with different intensity and time behavior. The collected datasets is included in an open data collection, i.e., Lampedusa Scintillation Monitoring Interfered Data (`LAMP_SMID_2109`),[3] and an overview of their time distribution over the test campaign is given in Table III .

B. Postprocessing Signal Analysis (SDR Data)

The binary files recorded at the station during the acquisition campaign were analyzed in postprocessing via a dedicated MATLAB framework. The proposed analysis was pursued to investigate the nature of the interferer and provide a preliminary characterization of the signal, as well as a quantification of its effect on the estimation of the S_4.

1) Spectral Analysis Through Power Spectral Density (PSD) Estimation: The analysis was performed through a PSD estimator, i.e., Welch spectrogram [58], [59], on signal snapshots with a duration of 1 s, and on the full capture of 10 min, according to

$$P_y(f) = \frac{1}{M}|\text{FFT}[y[n]]|^2 \triangleq \frac{1}{M}\left|\sum_{n=0}^{N-1} y[n]e^{\frac{j2\pi nk}{N}}\right| \quad (9)$$

where M is the amount of signal samples and N is the amount of evaluation point of the fast Fourier transform (FFT). The Welch PSD is, hence, given by averaging the periodogram as

$$S_y^W(f) \triangleq \frac{1}{K}\sum_{m=0}^{K-1} P_y(f) \quad (10)$$

where K is the amount of frames over which the power spectrum is averaged and W identifies the Welch formulation [58]. The analysis provided a preliminary feedback on possible spectral anomalies with respect to GNSS signals observed in nominal conditions.

2) Persistence Spectrum: This was adopted to investigate the RFI spectral signature and the stability of an intelligible PSD over short time periods [60]. This analysis is based on the accumulation of Welch spectrograms (9) on a grided PSD plot. The longer a particular PSD envelope persists in a signal as the signal evolves, the higher its time percentage and, thus, the brighter is the heatmap in the plot. The tool is also helpful to identify hidden coherent signals in noisy patterns as well as sporadic or fast pulsed signals with unknown duty cycles.

3) Time-Decimated Time–Frequency Analysis (TD-TFA): This was performed through the estimation of partially overlapping short-time Fourier transform (STFT). A signal chunk composed by N samples is filtered through a shaped window of length K, and a discrete Fourier transform (DFT) is computed over N_{DFT} points. The window slides over the next N samples with an overlap of the previous L samples, and a DFT is performed for each window. By sliding the window along the samples vector, a time–frequency analysis (TFA) provides a time–frequency view showing the evolution of the frequency content of a signal along the time [61]. The technique was exploited to describe the evolution of the signal by measuring its PSD profile over the whole acquisition time span. To reduce the size of the output data, a time decimation (TD) was performed by skipping a predefined time span in between subsequent signal chunks, with an acceptable reduction of the time resolution. Shorter signal time spans are preferable in terms of time consumption since they allow faster STFT computation, by dealing with smaller amounts of samples. In terms of the readability of the TD-TFA output figures, the following options provided similar results:

A. $t_i = 20$ ms and $t_s = 100$ ms $\rightarrow$ 285 MB
B. $t_i = 1$ s and $t_s = 1$ s $\rightarrow$ 28.5 MB

where t_i is the integration interval and corresponds to the overall duration of the signal samples processed through STFT, and t_s is the skip interval included between two subsequent integration intervals. While the first corresponds to the actual amount of input data, the latter indicates the duration of unprocessed signal chunks, thus representing the decimation factor of the proposed TD-TFA. TFA analysis contains more information in configuration A; however, this appeared not relevant as it does not significantly impact the visual detection of the interference signature in both time and frequency domains. Therefore, a suitable tradeoff between frequency, time resolutions, and storage occupancy of the TD-TFA output results was provided through the configuration B.

4) GNSS Signal Tracking: It was performed on the acquired datasets to quantify the impact of the RFI on GNSS receivers

[3][Online]. Available: http://ieee-dataport.org/10996

TABLE III
AMOUNT OF DATASETS COLLECTED DURING THE SEPTEMBER TEST CAMPAIGN IN LAMPEDUSA, AND AVAILABLE IN THE LAMP_SMID_2109 OPEN DATA COLLECTION

Date	Hour of the day (UTC)																							
	00	01	02	03	04	05	06	07	08	09	10	11	12	13	14	15	15	17	18	19	20	21	22	23
16-September-2021																				6				
17-September-2021	1[a]			6	6										6	6	6	6	6			5	6	5
18-September-2021	6	6		6	6	6	6													6	6	6	6	6
19-September-2021	6	6	5	6		5																		
27-September-2021																				6			6	

[a]Reference dataset not automatically retrieved by the system but still affected by low-intensity RFI.

tracking stage, thus assessing the induced jamming effect on navigation signals in terms of C/N_0. The signal tracking leverages the cross-correlation of direct-sequence spread spectrum (DSSS) code division multiple access (CDMA) signals transmitted by GPS and Galileo satellites. The software receiver architecture imitates the conventional channel tracking already described in Fig. 2. For the scope of these analysis, the tracking was performed on the acquired GNSS signals with a coherent integration time $T_c = 0.020$ s. A key metric for the conditioning of S_4 is the C/N_0 measured at each channel. According to the analysis presented in Section III, common effects are expected to be concurrently observed on different satellites signals. Therefore, we propose an aggregate estimation of the variation of C/No, namely, $\delta C/No$, with respect to the mean value used in (7). Formally, an estimate of the C/No is given by

$$C/N_0 = 10\log_{10}\left(\text{SNR}B_{eq}\right) \tag{11}$$

where $B_{eq} = 1/Tc$ with T_c stands for the coherent integration time, and

$$\text{SNR} = \frac{1}{2\tilde{}M}\sum_{i=0}^{M}\frac{\left(|I_i| - |Q_i|\right)^2}{I_i^2 + Q_i^2}. \tag{12}$$

The C/N_0 is, hence, computed over a window of length M that is typically set to $1/T_c$. To be consistent with the definition of the indices provided in Section II-B, its aggregated variation for all the tracked signals has to be measured by averaging the 60 s detrended series of the respective C/N_0 (11), as

$$\delta C/N_0 = \frac{1}{S}\sum_{j=0}^{S}\left((C/N_0)_W^{(j)} - \langle (C/N_0)^{(j)}\rangle_W\right) \tag{13}$$

where j refers to the jth GNSS signal, $W = 60$ s indicates the observation window, and S refers to the overall number of available signals.

5) RFI Signal Emulation and Model: Provided the features observed through the abovementioned analysis tools and the recent literature on GNSS interferences and threats, a signal with similar features was numerically simulated and reproduced by means of a MATLAB routine.

C. Analysis of the GISTM Scintillation Data

1) Ground-Based Scintillation Climatology (GBSC): It consists in building maps of the percentage occurrences of the scintillation indices above a predefined threshold and evaluated over a certain time period [2]. The climatological maps report the percentage occurrences on a bidimensional time-grid having the hour of the day in the horizontal axis and the day of the year in the vertical one or as geographic maps, showing the percentage occurrences evaluated over geographic cells with a given spatial resolution. The technique is used to perform climatological analysis of scintillation events, but it can also be adopted to highlight the spatial and temporal features of scintillations over shorter time periods (e.g., few months). With regards to the S_4 index, the S_4 percentage occurrences in a given time interval ($S_{4\text{POt}}$) is evaluated as

$$S_{4\text{POt}} = \frac{S_{4\text{thr}}(\Delta t)}{S_{4\text{tot}}(\Delta t)} \tag{14}$$

where $S_{4\text{thr}}(\Delta t)$ is the total number of the S_4 occurrences above the chosen threshold in the given time interval Δt and $S_{4\text{tot}}(\Delta t)$ is the overall number of S_4 measurements available in the same time interval. The S_4 percentage occurrences over a specific geographic cell ($S_{4\text{POs}}$) is evaluated as

$$S_{4\text{POs}} = \frac{S_{4\text{thr}}(\Delta t, \Delta\text{lat}, \Delta\text{lon})}{S_{4\text{tot}}(\Delta t, \Delta\text{lat}, \Delta\text{lon})} \tag{15}$$

where $S_{4\text{thr}}(\Delta t, \Delta\text{lat}, \Delta\text{lon})$ is the total number of the S_4 occurrences above the chosen threshold in the given time interval Δt and limited to the specific geographic cell (range of latitudes Δlat and longitudes Δlon), while $S_{4\text{tot}}(\Delta t, \Delta\text{lat}, \Delta\text{lon})$ is the overall number of S_4 measurements available in the same time interval and pertaining the same geographic cell.

2) RFI Filtering: In order to remove the RFI-induced anomalies from the S_4 data, all the epochs in which the mean values of the S_4 (calculated on all the available signals at that epoch) are above a certain threshold have to be filtered out from the dataset; indeed, as follows from the considerations reported in Section III-B, the RFI has the effect of increasing the S_4 values of the majority of the satellites in view at the same epoch, differently from actual ionospheric scintillation events. In the case of Lampedusa, given that the average number of satellites simultaneously in the FoV above 10° of elevation is 30, and assuming that 20% of the signals could be at most simultaneously affected by actual ionospheric scintillations at these latitudes, a threshold of 0.15 for the mean values of the S_4 has been chosen as a good compromise to detect most of the RFI-induced anomalies, avoiding at the same time to filtering out possible actual ionospheric scintillation events. It has to be noted, however, that the proposed filtering technique potentially removes from the dataset the actual ionospheric scintillation events occurring contemporary the interferences.

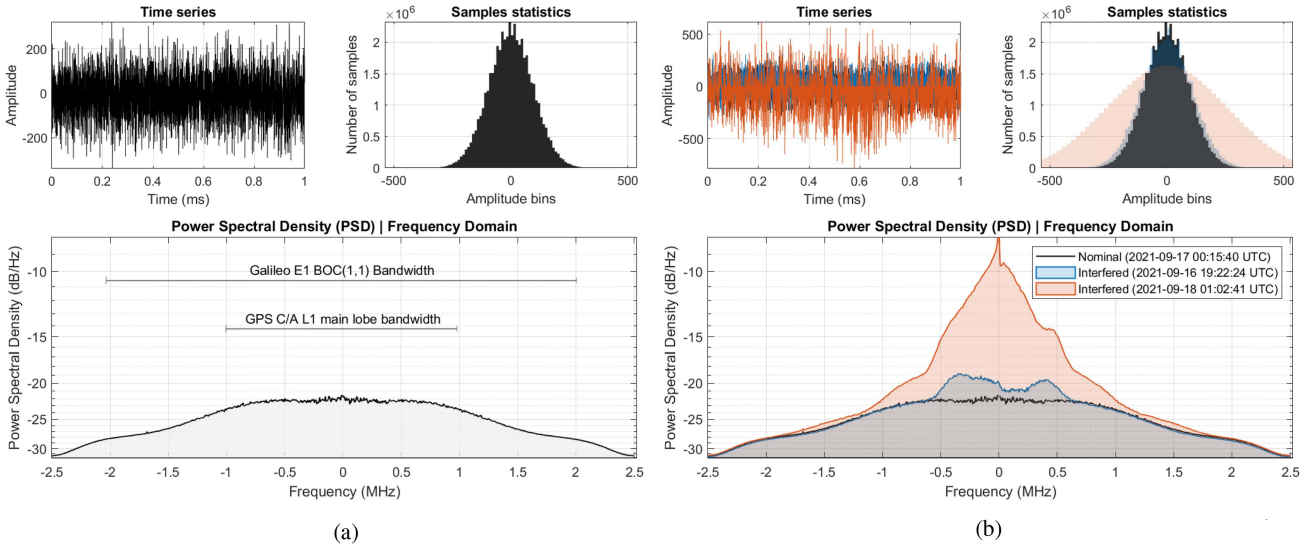

(a) (b)

Fig. 8. Single and multiple datasets data probing performed on 1 s signal chunks by means of a GNSS signal analysis tool embedded in the GNSS software receiver. (a) Single dataset: signal characterization in nominal conditions. (b) Multiple datasets comparison in nominal and interfered conditions.

TABLE IV
DATASETS SELECTED AS REPRESENTATIVE SAMPLES OF THE OBSERVED ANOMALOUS GNSS SIGNALS FOR THE PRESENTATION OF THE ANALYSIS RESULTS IN SECTION V-A

ID	Date	Start time (UTC)	End time (UTC)	max(S_4)
(a)	16-September-2021	19:22:24	19:33:00	0.63
(b)	17-September-2021[b]	00:15:40	02:26:00	0.17
(c)	18-September-2021	01:02:41	02:13:00	0.43
(d)	19-September-2021[b]	02:20:07	02:31:00	0.18
(e)	19-September-2021	05:12:02	05:22:00	0.38
(f)	19-September-2021	05:42:22	05:52:00	0.32

[b] Datasets not kept by the automated grabbing system.

V. RESULTS

A. Characterization of the RFI

This section provides a first characterization about the RFI through the analysis tools presented in Section IV-B. For the sake of conciseness, the datasets listed in Table IV have been considered as representative samples of the RFI behavior in different conditions.

1) Spectral Analysis Through PSD Estimation: Fig. 8(a) and (b) compares time series (top-left), samples histograms (top-right), and PSD (bottom) of 1 s signal snapshots belonging to three different datasets. In Fig. 8(a), a dataset observed in 17-September-2021 with nominal PSD (when no interference was detected) is reported and compared in Fig. 8(b) with two interfered power spectra acquired during 16-September-2021 and 18-September-2021 From the time series and the samples histogram of Fig. 8(b), we observe that additional power provided by the RFI in 16-September-2021 was not significantly higher than in nominal conditions (around 3 dB); a more powerful RFI event is provided by the RFI in 18-September-2021 that visibly affect time series and histograms, and shows a more evident power density distortion in the observed bandwidth. The plot assesses the presence of a nonnegligible interference lobe with a peak of about 10 dB of additional power density in the PSD (with respect to the nominal level observed in 17-September-2021). In regular conditions or under natural phenomena, such as ionospheric scintillations, GNSS signals are typically not affected by similar, significant variations in the observed PSD. A strong continuous wave peak appears at the center frequency 1575.42 MHz (GNSS L1/E1 Bandwidth) and can be occasionally visible in the figures; this tone is due to a spectral leakage of the local oscillator operating at frequency f_c in the ER USRP N210 front-end and it does not affect nor invalidate the analysis. It has been verified that the leakage is not a component of the RFI.

2) Spectral Persistency and RFI Spectral Signature: The set of plots in Fig. 9 shows examples of persistent spectrum analysis performed on 1 ms signal chunks every 10 s for an overall observation time of 60 s. As we can observe through the subplots, the spectral signature of the interferer considerably changes along the time. A nearly symmetrical spectral signature is visible in Fig. 9(d) that may suggest a two-frequency shift keying (FSK) modulation. However such a signature slightly recurs only in Fig. 9(b) with a lower intensity, thus weakening the hypothesis. Similar asymmetrical signatures can be observed in Fig. 9(a) and (e). A flattened spectral shape is instead visible in Fig. 9(c) and (f) where RFI intensity dramatically drops. Such a time-varying behavior makes the signal particularly difficult to be automatically identified, or tracked. In addition, autocorrelation of time series along the observed datasets did not show any relevant similarity of the signal with itself, nor evident cyclic or recurrent components such as spreading codes or synchronization preambles. These features turn into strengths for malicious signals to not be tracked or automatically detected. In light of this, the RFI assumes the characterization of an unstructured interference.

3) Time–Frequency Analysis: TD-TFA applied on the datasets of Table IV is shown in Fig. 10.[4] In line with the

[4] Date and time are detailed in the subcaptions, and data are limited to 9 min as 30 s, respectively, discarded at the beginning and at the end of the data collection to avoid undesired transients.

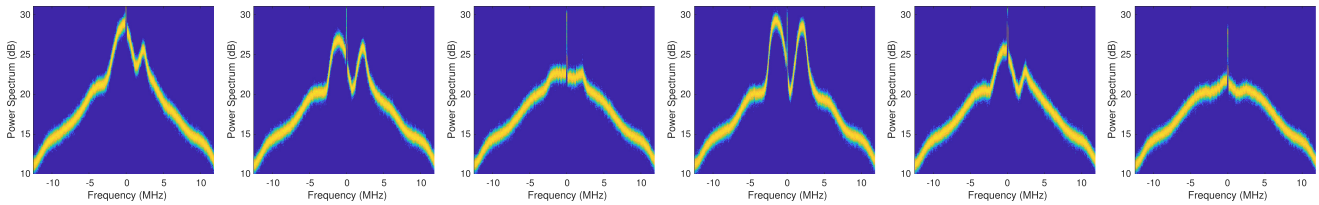

Fig. 9. Examples of persistence spectra computed for 1 ms signal chunks observed every 10 s to highlight RFI spectral signature stability over 50 s timespan (subplot a to f). Sample dataset captured on 18-September-2021 01:02:41 AM. Frequency resolution: 97.7517 kHz and time resolution: 781.28 μs.

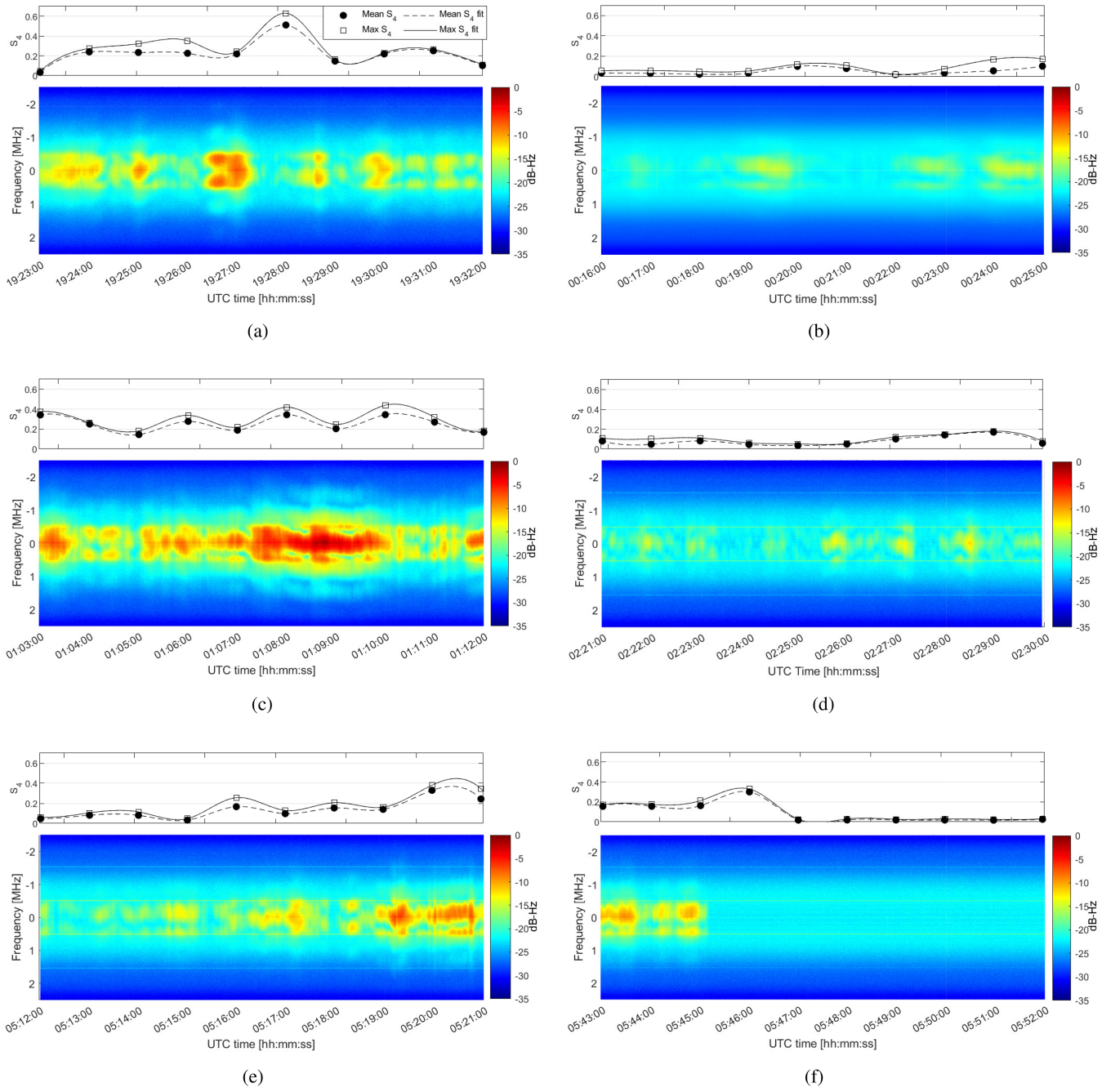

Fig. 10. TD-TFA of the datasets in Table III showing different RFI behaviors in terms of PSD time evolution, compared with maximum and mean S_4 time series (top panels). Filled and blank markers indicate mean and maximum S_4 values, respectively (top panels). Spectrograms and S_4 data series are obtained from independent devices. (a) 16-September-2021 19:22:24 UTC. (b) 17-September-2021 00:15:40 UTC. (c) 18-September-2021 01:02:41 UTC. (d) 19-September-2021 02:20:07 UTC. (e) 19-September-2021 05:12:02 UTC. (f) 19-September-2021 05:42:22 UTC.

parameters described in Section IV-B3, we set the window length $K = 1\,\text{s} \cdot 10^6$ Msps, a number of DFT points $N_{\text{DFT}} = 2^10$, a rectangular window of length $K = N_{\text{DFT}}$, and an overlap $L = 2^6$. As a term of comparison, the figures show in the top panels of each plot the cubic interpolation of both maximum and mean S_4 values computed by the GISTM receiver, and aligned according to the UTC time of the records. The colorscale of the PSDs is referred to the maximum observed S_4 intensity within the overall data collection (i.e., 0 dB-Hz). Frequency axis in the plots, i.e., y-axis, is centered at the target frequency, i.e., 1575.42 MHz, referred to as 0 Hz, and time scale is reported in 24-h format. Irregular PSD behavior is observed in time for all the collected datasets, and RFI's intensity shows a remarkable variability during the observation time spans. Furthermore, in all the datasets, the RFI is visibly limited in the bandwidth of $\pm$0.5 MHz. In the case of low-power interference shown in Fig. 10(d), the RFI is visible but its effect is not reflected on the scintillation index (S_4 index below the defined threshold). The dataset was kept and analyzed before being automatically discarded by the system in order to provide a term of comparison for more intense RFI phenomena. It is worth observing that the effects on S_4, induced by RFI's PSD variations, are delayed of 60 s due to the accumulation of I_p and Q_p samples over 60 s observation time spans. In Fig. 10(a), we observe intense power density fluctuations with an intensity peak (-5 dB-Hz) at about 19:27:00. Two spectral lobes are visible in the first half of such a high-intensity interval. Fig. 10(b) shows a minimal intensity interferer where the aforementioned, peculiar spectral features are visible mostly between 00:18:00 and 00:20:00 and after 00:22:00. Recorded PSD reached a peak of -15 dB. Fig. 10(c) shows the most intense RFI action, where the received power reached a maximum in between -5 and 0 dB-Hz in the interval between 01:08:00 and 01:10:00. Peak intensity caused spurious interference out of assumed RFI bandwidth, being possibly detrimental for Galileo E1 signals. Fig. 10(d) shows a fragmentation of the RFI PSD with an unusual behavior and mid to low intensity sporadic peaks were observed in the second half of the dataset. Fig. 10(e) shows an increasing RFI intensity with time that reaches its maximum (-5–0 dB-Hz) by the end of the dataset. The dataset presents a unique example of regular intensity growth. Fig. 10(f) shows a sharp drop in the received RFI power density at about 05:45:30. The phenomenon suggests a sudden interruption of the RFI transmission. In the first quarter of the plot, the PSD shows moderate to strong intensity in the range -10 to -5 dB-Hz. Additional continuous wave (CW) interferences were sporadically observed, such as in Fig. 10(d)–(f) with a nonnegligible intensity at $\pm$0.5 MHz and $\pm$1.5 MHz. However, their presence cannot be directly related to the RFI target in this study. It is worth remarking that power variations highlighted by TFA appear slower than the changes observed in the spectral signature, thus we cannot assume they are related.

4) C/N_0 Estimation in GNSS Receiver Open-Loop Tracking Stage: According to the theoretical definitions of corrected amplitude ionospheric indices provided in Section II-B, the impact of rapid C/N_0 fluctuations induced by the RFI may cause misleading output values at GISTM. The following results show a more accurate match among such abrupt variations of the estimated C/N_0 and the anomalous increments of the corresponding amplitude scintillation index S_4 computed by the GISTM receiver. Noisy data series are obtained through (13), and they are plotted along with their 95% confidence interval (shaded gray areas). The plots presented in Fig. 11 show the variation of the C/No, namely, $\delta C/N_0$, with respect to its mean estimated over nonoverlapping windows of 60 s for the selected datasets. By comparing the results with the TFA analysis of Fig. 10, it can be seen that in correspondence of intense RFI occurrences, rapid fluctuations of the C/No are present, thus they have not been properly compensated in the computation of $S_{4,n}$ through (7). Despite this effect is more evident for GPS L1/CA records, intense RFI occurrences also lead to remarkable fluctuations in Galileo E1c data.[5] More in detail: Fig. 11(a) shows the strongest fluctuations both in GPS and Galileo E1c signals. Peaks overcome a range of $\pm$5 dB up to severe drops of -8 dB for GPS L1/CA and confidence interval appears larger in correspondence of the main peak. Fig. 11(b) shows few fluctuations on GPS L1/CA C/No estimates in the range of $\pm$3 dB. No relevant effects are observed on Galileo signals. The example confirms that low-intensity RFI may not severely impact S_4 estimation but they still induce perturbation in the estimated C/N_0 and may impact the performance of GNSS receivers. Fig. 11(c) shows intense fluctuations of Galileo E1c C/N_0 estimates in the range of $\pm$4 dB with remarkable C/N_o drops reaching approximately -5 dB between 01:07:00 and 01:09:00 UTC. GPS L1/CA C/No estimates appear slightly affected in this case, but it shows a larger confidence interval in correspondence to the peak RFI intensity of Fig. 10(c). This highlights a higher variability of the RFI effect on the different GNSS signals. Fig. 11(d) is a further example of poorly invasive RFI with constrained fluctuations in the range $\pm$3 dB. After 02:26:00 UTC, we observe a moderate increment of S_4 being reasonably attributed to the fluctuations in GPS L1/CA and Galileo E1c C/N_0 estimates. Fig. 11(e) shows increasing fluctuations of the $\delta C/N_o$ in both GPS L1/CA and Galileo E1c estimates. The strongest impact is visible for GPS L1/CA with values overcoming the range of $\pm$5 dB as well as remarkable enlargement of the confidence interval since about 05:16:00 UTC. Fig. 11(f) shows a sudden drop in the RFI intensity at about 05:46:00 UTC. Such a peculiar behavior was already shown in Fig. 10(f), and it further clarifies the direct effect of the RFI on the C/N_0 estimation. S_4 reacts immediately to the quick fluctuations while assumes near-zero values by the end of the phenomenon. Until about 05:46:00 UTC, both GPS L1/CA and Galileo E1c signals show severe fluctuations in the range of approximately $\pm$4 dB. The estimated average C/N_0 in GPS L1/CA also shows a larger confidence interval in correspondence of local maxima and minima.

B. RFI Numerical Emulation

Relying on the TD-TFA, it can be inferred that no patterns can be recognized both in the temporal evolution of the signal and

[5] $\delta C/No$ and S_4 data series are obtained from independent devices.

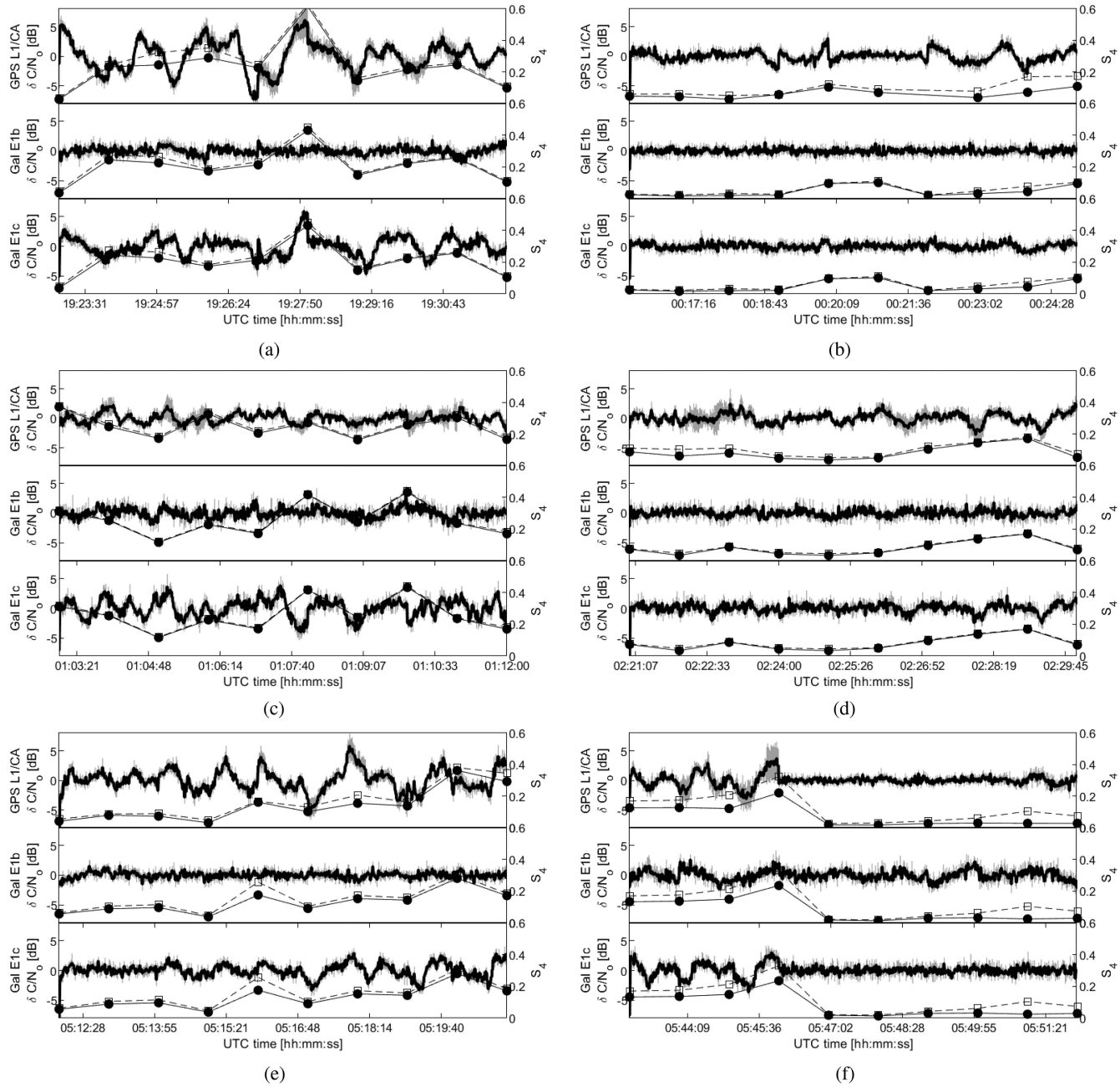

Fig. 11. Mean variation of the estimated C/N_0 (13) for GPS L1/CA, Galileo E1b, and E1c during the observation time spans of the selected datasets (limited to 9 min). Filled and blank markers indicate mean and maximum S_4 values, respectively (magnitude on the right y-axis). Background, gray-shaded areas show the 95 % confidence interval (left y-axis). (a) 16-September-2021 19:22:24 UTC. (b) 17-September-2021 00:15:40 UTC. (c) 18-September-2021 01:02:41 UTC. (d) 19-September-2021 02:20:07 UTC. (e) 19-September-2021 05:12:02 UTC. (f) 19-September-2021 05:42:22 UTC.

in its spectral content. Furthermore, RFI received power shows slow variations and a generous intensity range. TD-TFA was fundamental to observe that the RFIs occurrences may show a sharp starting and ending time that can be easily attributed to artificial, deliberate transmissions. Relying on these observations, the most relevant information that justify the modeling we propose hereafter comes from the persistence spectral analysis and from background literature on communication systems and GNSS threats and mitigation. A basic model for a multiple FSK (MFSK)/frequency-hopped (FH) signal was implemented to be compared with the identified RFI and foster the design of new countermeasures to mitigate its action. Despite of being a conventional modulation scheme for communication channels, multiple FSK (MFSK) has been employed in radar applications for its capacity of measuring and resolving targets in range and Doppler frequency simultaneously and unambiguously even in multitarget situations [62]. A MATLAB script was exploited to numerically evaluate the expression

$$x_{\text{RFI}}[n] \triangleq x_{\text{RFI}}(nT_s) = A \sum_{m=1}^{W} e^{j2\pi f_m(nT_s)nT_s} \tag{16}$$

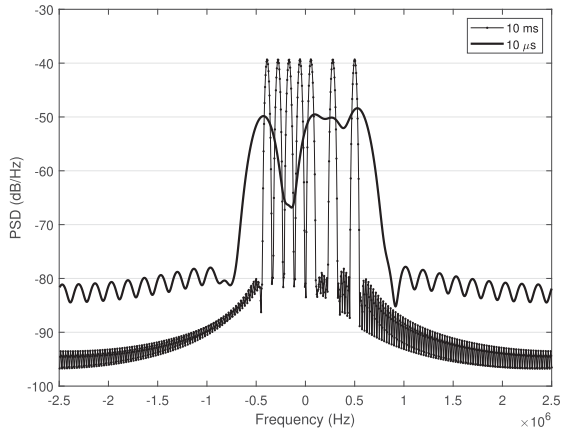

Fig. 12. PSDs of a simulated MFSK transmission observed over different snapshots duration and acting as an FH jamming interference. The spectral signature shows remarkable similarities with respect to the RFI's counterpart in Figs. 8 and 9. Lower noise floor is considered with respect to the collected data.

TABLE V
SIMULATION PARAMETERS FOR THE EMULATION OF A MFSK/FH JAMMING SIGNAL

Symbol	Definition	Value
f_0	Center frequency	1575.42 MHz (L1)
f_s	Sampling frequency	5 Msps
T_x	Signal duration	10^{-3} s (10 ms)
M	Subcarriers	10
W	Random generation trials	3
R_f	Subcarriers range	± 0.5 MHz

where $f_m(nT_s)$ is a function that randomizes the generation of a set of m subtones included in a predefined frequency range, T_s is the sampling interval, A is the signal amplitude, and n is the discrete time index. The randomization of the subtones may reflect a set of random symbols carrying the data of an actual data transmission. The plot in Fig. 12 shows an example of a numerically generated MFSK/FH jamming signal over a null-to-null bandwidth of about 1 MHz, by randomly switching among 10 subtones equally spaced in the range ± 0.5 MHz with an overall duration of 10 ms. Simulation settings are summarized in Table V for repeatability. It can be noticed that spectral estimation over longer observation time, e.g., 10 ms, highlights the active subtones while shorter time spans prevent a detailed characterization of the spectral signature. By inducing a periodical change of the selected subtones, the signal would behave similarly to a randomized variant of a FH tick jammer described in [63], with a simpler spectral signature of the tones. The randomization of the tones allows to reduce autocorrelation and signal ergodicity. Discontinuities are, hence, introduced in the instantaneous frequency of the jamming signals. Such discontinuities reduce the effectiveness of adaptive mitigation techniques based on adaptive filtering (e.g., adaptive notch filters), which may be unable to track the jamming signal. The designed MFSK signal shows frequent and remarkable changes in its spectral signature, as shown in Fig. 13, where the numerical RFI shows a similar behavior to the one observed in persistence spectra analysis of Fig. 9, in Section V.

C. Impact of the RFI on Scintillation Data and Filtering Algorithm

1) Effects of the RFI on Low-Latitudes Ionospheric Scintillations Investigation: As mentioned in Sections I and III, mid-latitudes scintillation may occur as a consequence of disturbed space weather conditions; on the contrary, low-latitude scintillations are also possible during quiet time, especially for the geomagnetic latitudes close to the northern and southern EIA crests, due to the formation of small scale irregularities embedded in the EPBs. Considering the position of the Lampedusa observatory, an investigation addressed to the observation of low-latitude scintillations would require to also include the signals coming from low-elevation satellites with respect to the receiver FoV; this will introduce additional outliers in the data due to the effects of the multipath, as mentioned in Section III. In the analysis that follows an elevation mask of 10° and an azimuthal mask between 90° and 270° was applied to the signals in view, thus focusing on the middle and low latitudes between 24.6°N and 36°N and on a longitudinal sector between 1°W and 26°E. The investigated time period goes from 1 July, 2021, to the 31 October, 2021, thus including the period of the equinox, when EPBs are more likely to occur. The considered signals are the one belonging to the GPS, Galileo, BDS, and GLONASS constellations. The reported S_4 are the slant values calculated from the L1/E1 frequency band for each satellites in view at 1-min resolution.

According to the methodology described in Section IV-C1, the image of Fig. 14(a) shows the percentage occurrences of the S_4 index ($S_{4\mathrm{PO}t}$) above the threshold of moderate scintillation ($S_4 > 0.25$) on a bidimensional time-grid reporting the hour of the day in the horizontal axis and the day of the year in the vertical one. Each IPPs' epoch is converted in local time and the $S_{4\mathrm{PO}t}$ are calculated according to (14) over the whole FoV under investigation and for time intervals of 4 min. In Fig. 14(a), the white line represents the solar terminator at 350 km (F-layer of the ionosphere), which may help to identify postsunset scintillation due to EPBs. As it is possible to see from Fig. 14(a), two pronounced features are visible: the first one is due to the effect of the multipath, recognizable by the oblique stripes in the background due to the joint effect of the satellites' ground track, the fixed position of the reflecting obstacles and the time-difference between the solar and sidereal day. The second one consists in the brighter horizontal stripes, due to the effect of the RFI on the signals collected by the receiving antenna. Indeed, since the RFI affects the S_4 index of most of the satellites in view simultaneously (as shown in Section III), the anomalous occurrences can be recognized by looking at the highest values of the $S_{4\mathrm{PO}t}$ in Fig. 14(a), which suggest the presence of the interferer also in the data collected during the month of July and September (besides August, investigated in the preliminary analysis of Section III). Fig. 14(b) reports on a geographic map the percentage occurrences of the S_4 ($S_{4\mathrm{POs}}$) calculated according to (15) over the whole time period under investigation and for geographic cells of $1° \times 1°$ spatial resolution. Fig. 14(b) shows that the entire FoV under investigation appears to have been subject to scintillations during the investigated time period;

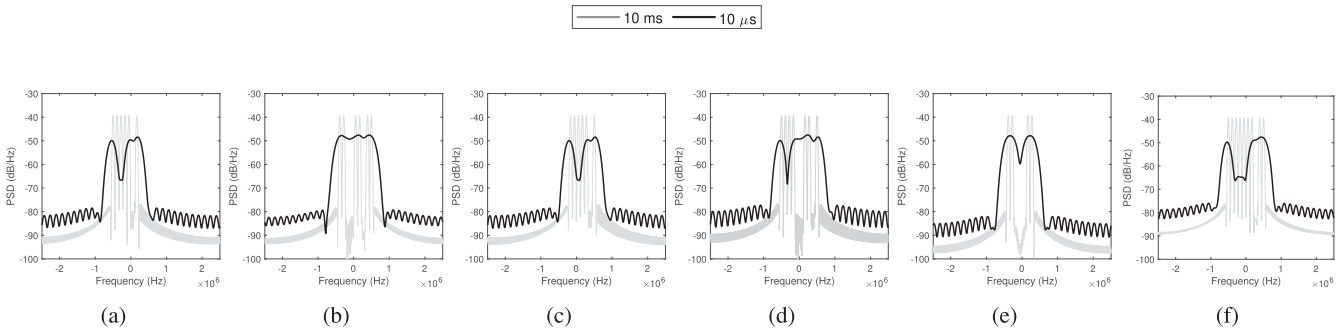

Fig. 13. Example of the evolution of the signal PSD of the emulated RFI. Different frequency resolutions are achieved by spectral estimation performed on different durations of the signal chunk under analysis, i.e., 10 ms (light-gray lines) and 10 μs (black lines). As in Fig. 9, subplot a to f reports a series of PSDs obtained by observing 1 ms signal chunks every 10 s over a 50 s timespan.

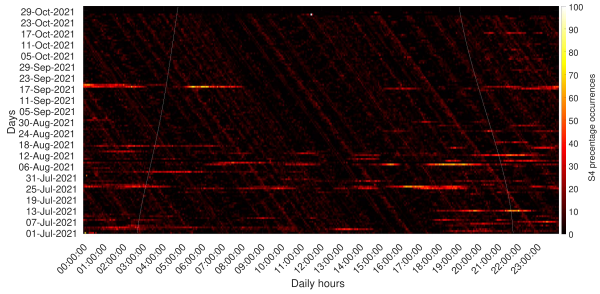

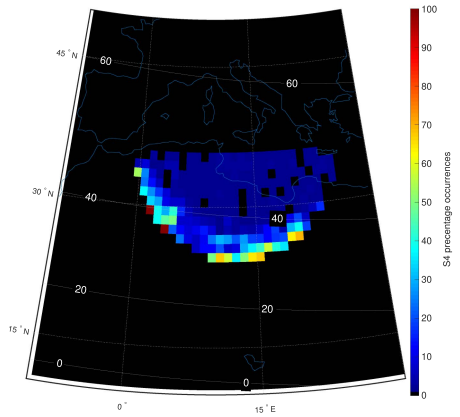

Fig. 14. (a) $S_{4\mathrm{POt}}$ and (b) $S_{4\mathrm{POs}}$ above the threshold of moderate scintillation ($S_4 > 0.25$) between July and October 2021. The white lines of (a) represent the solar terminator at 350 km. In (b), geographic coordinates are labeled at the border of the maps and represented by the dotted lines inside the map; geomagnetic latitudes are labeled inside the maps and represented with the continuous lines.

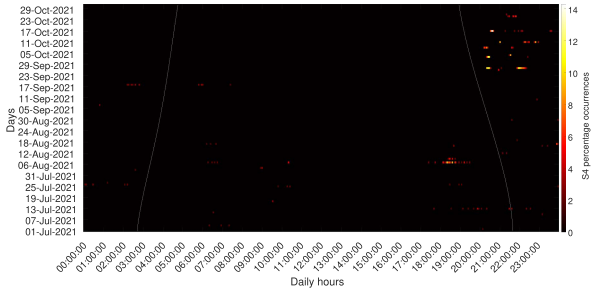

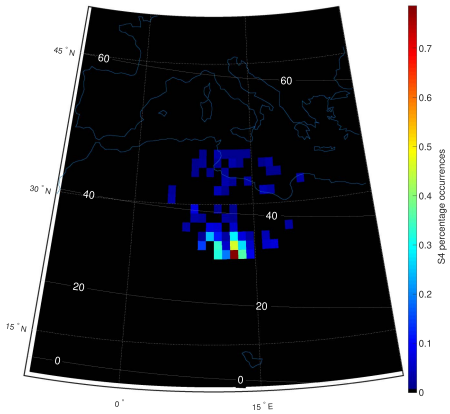

Fig. 15. (a) $S_{4\mathrm{POt}}$ and (b) $S_{4\mathrm{POs}}$ above the threshold of severe scintillation ($S_4 > 0.7$) between July and October 2021. The white lines of (a) represent the solar terminator at 350 km. In (b), geographic coordinates are labeled at the border of the maps and represented by the dotted lines inside the map; geomagnetic latitudes are labeled inside the maps and represented with the continuous lines.

this is also a consequence of the RFI, which affects most of the signal in the FoV (see Section III). Instead, the stronger $S_{4\mathrm{POs}}$ values of Fig. 14(b) are mostly due to the multipath, which affect the signals coming from the low-elevation satellites.

Being not possible to exclude the low-elevation satellites (due to the necessity of observing low latitudes), a possible way to remove the outliers produced by the multipath is by increasing the threshold of the S_4 occurrences above the level of severe scintillation ($S_4 > 0.7$); this operation has also the beneficial effect of removing the less intense S_4 anomalies caused by the RFI, but will prevent the capability to detect possible real ionospheric scintillations events of moderate intensity. The result of this operation is shown in Fig. 15: the background feature due to the multipath visible in Fig. 14(a) is removed [see Fig. 15(a)] and the overall spatial and temporal extent of the anomalies induced by the RFI is minimized as expected [see Fig. 15(a) and (b) in comparison to Fig. 14(a) and (b)].

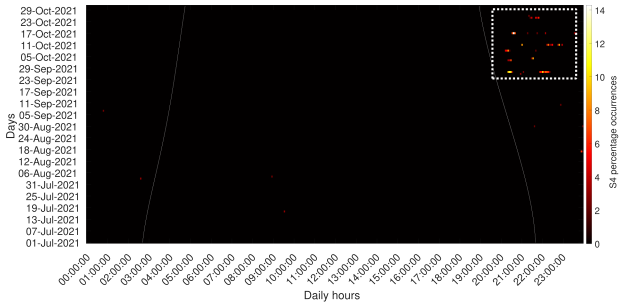

(a)

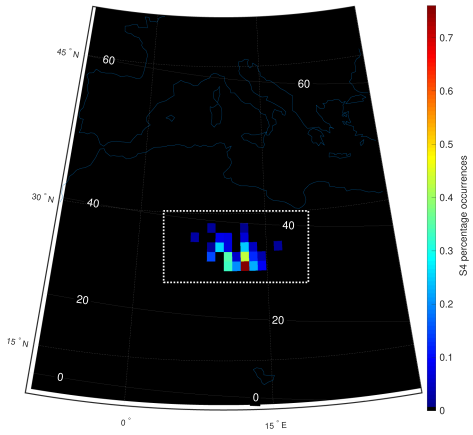

(b)

Fig. 16. (a) $S_{4\mathrm{POt}}$ and (b) $S_{4\mathrm{POs}}$ above the threshold of severe scintillation ($S_4 > 0.7$) between July and October 2021 after applying the filter for the RFI removal. The white lines of (a) represent the solar terminator at 350 km. In (b), geographic coordinates are labeled at the border of the maps and represented by the dotted lines inside the map; geomagnetic latitudes are labeled inside the maps and represented with the continuous lines. The white dotted boxes highlight ionospheric scintillation events due to EPBs.

2) RFI Filtering and Detection of Ionospheric Scintillation Events: The S_4 percentage occurrences reported in Fig. 15 are due to both RFI-affected observations and possibly actual ionospheric scintillation events. To finally detect and remove the remaining S_4 anomalies due to the severe effect induced by the RFI, it is possible to reprocess the original data according to the methodology reported in Section IV-C2. The result of this filtering operation is shown by the images of Fig. 16. By detecting and removing the occurrences attributed to the RFI, the timeline of the $S_{4\mathrm{POt}}$ reported in Fig. 16(a) allows to detect, without ambiguities, severe scintillation events (highlighted by the white dotted box) occurred in the postsunset hours during the period of the autumn equinox 2021. Similarly, the map of Fig. 16(b) reports the $S_{4\mathrm{POs}}$, showing the actual geographic area affected by scintillations (highlighted by the white dotted box), which cover the lowest latitudes in the FoV. The scintillation events highlighted in Fig. 16 reflect the typical features of ionospheric scintillations induced on GNSS signals by small scale irregularities embedded in EPBs reaching the north crest of the EIA. Even though an accurate characterization of these phenomena falls outside the scope of this article, the reported

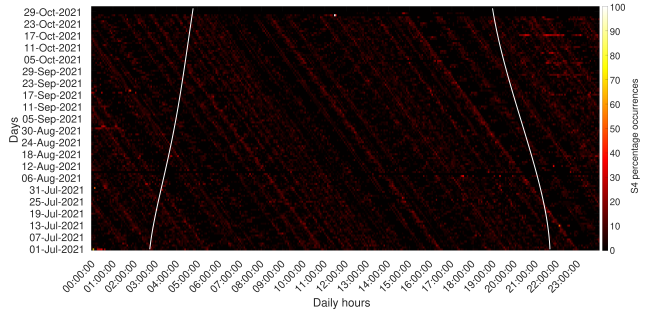

Fig. 17. $S_{4\mathrm{POt}}$ after applying the filter for RFI removal on the data of Fig. 14(a).

analysis allows to emphasizes how unrecognized RFIs would have triggered false scintillation alarms on several occasions [see Fig. 15(a) compared with Fig. 16(a)] and above incorrect locations [(see Fig. 15(b) compared with Fig. 16(b)]; this poses a threat for the reliability of real-time ionospheric scintillations monitoring application as well as for the integrity of scientific investigation addressed to ionospheric scintillation climatology. To conclude, the performances of the proposed filter are also highlighted in Fig. 17, which shows the result of the RFI-filtering operation before the mitigation of the multipath (data of Fig. 14), thus also including the anomalies causing moderate effect on ionospheric scintillation ($S_4 > 0.25$). The comparison between Figs. 17 and 14(a) highlights the capability of the procedures to effectively detect and remove the anomalies due to the interferer.

VI. Discussion

No natural events or human, licit or illicit activities being known to the authors seem related to the anomalous occurrences and the features of the disturbance. In addition, no other instruments were expected operating in GNSS L1-band at the ENEA station or can interfere by emitting spurious harmonics in such a frequency range. The RFI may be generated in the proximity of the GISTM station (jamming or self-jamming) through a fixed or moving transmitter but the slow, yet remarkable power variations may indicate variable distance or heading of the transmitting antenna. This feature may be attributed to a moving transmitter carried on board of a plane, ground vehicle, or ship (mobile transmitter with fixed/moving antenna). Independently on the dynamics of the emitter, the RFI transmitting antenna may change its orientation along the time (e.g., fixed emitter with a spinning antenna as per radar applications). However, nor the regularity of the power fluctuation nor evident duty cycles in the received power suggest the possibility of a regularly spinning antenna. In light of this, the hypothesis of a moving emitter appears more reasonable. We cannot exclude the presence of jamming activities in the area of interest, as well as the possibility of experimental tests for MFSK radar systems or undocumented applications such as steganography in GNSS band for stealth data transmission. In fact, the characterization of the RFI detected in Lampedusa reflects the features of a deliberate MFSK transmission that may occasionally turn into a jamming interference on the L1/E1 frequency band in the case of intense received signals. It mainly affects and severely degrades GPS

L1/CA and Galileo E1c signals, but it seems poorly effective as a jammer against Galileo E1b, GLONASS, and Beidou signals; in light of this, the gathered clues suggest that the observed RFI may constitute a rough attempt of RF steganography covered by GNSS signals or a modern FH jammer. As a general remark, similar transmissions over GNSS L1/E1 center frequency are generally forbidden. However, while the United States prohibits unauthorized transmission on the GNSS frequency bands by federal laws [64], European regulations are more fragmented and may differ among member and non-member states. Specifically, the Italian legislation, with articles 340, 617, and 617 bis of the Penal Code, punishes the use and installation of jamming devices. In Italy, the deliberate use of interferers is allowed only to law enforcement and military forces, but the limitations at the continental border between Europe and Africa, such as in the area of Lampedusa, may not be exhaustively disciplined by regulations. Nonetheless, their occurrences are growing worldwide and at the European borders they might be due to the intensification of war actions and the presence of military enforcement. Therefore, an increasing attention is nowadays placed on their effects on several civil GNSS-related activities, such as flight operations, maritime navigation, and critical infrastructures. A remarkable effort is, indeed, being placed toward RFI monitoring and localization by means of LEO satellites [44], [65]. From a terrestrial perspective, the deployment of multiple synchronous stations would allow as well for time difference of arrival (TDOA)/frequency difference of arrival (FDOA)-based interfere localization [66], [67], [68]. At the time of writing, RFI localization falls outside the scope of this article. Despite the interferer detected in Lampedusa is, at the moment, of unknown origin, its appearances during summer periods and the geopolitical conditions of the area make it possibly related to the migratory flows phenomena involving the surrounding seas, from the African coast to the east Mediterranean.

With regards to the scientific activities, recent discussions in the ionospheric community have raised the attention about the possible disruptive effects of RFIs on the data collected for scientific investigations of the ionosphere as well as for space weather monitoring applications. This article provided an on-field proof of such vulnerabilities, showing the adverse impact of RFIs for both near-real-time GNSS scintillation events detection as well as in the case of climatological investigations of ionospheric scintillations. In the case of Lampedusa, the intensity and repetition over time of the S_4 anomalies allowed to promptly acknowledge the presence of a possible source of interference; however, similar but less impacting RFIs may not be easily recognizable and yet affecting the quality of the collected data. At the same time, deploying capturing systems to detect and characterize RFIs, such as the one presented in this study, is not a sustainable solution for both economical and technical aspects. At the time of writing, no real-time mitigation techniques for such elaborate interferers are known to the authors, and only a posteriori processing may allow to detect interfered observations and provide quality metrics for the collected data. In this regard, this work proposed a preliminary postprocessing methodology to detect and remove the RFI-induced anomalies from the scintillation data acquired by the GISTM receiver. The filter is not based on the specific characteristics of the RFI under investigation and, in principle, it can be also effective for different types of RFIs acting within the GNSS bandwidths; however, it has the bottleneck of being based on a threshold, which is defined through a priori assumptions and which is location dependent. The design of more robust postprocessing algorithms falls outside the scope of this article and deserves dedicated investigations.

Summarizing, the lack of an accurate RFI model constitutes the main concern for a systematic analysis of its impact on the scintillation index. Besides, it is worth pointing out that a methodology to evaluate the RFI impact on the scintillation index is also lacking in the literature, and it deserves dedicated investigations in future works.

VII. Conclusion

This article presented an investigation of a real scenario where an unclassified RFI affecting the GNSS signals jeopardize scientific activities, such as those carried-out by the INGV in the Mediterranean area of Lampedusa. It was shown that the computation of the ionospheric scintillation indices through modern commercial GISTM receivers may be misleading in those circumstances, thus triggering false ionospheric scintillation events and compromising the reliability of real-time monitoring applications as well as the quality of the data collected for scientific investigations. The analysis presented on the recorded GNSS signals specifically demonstrated that altered scintillation indices may be due to the nonstationarity of the estimated C/N_0 caused by the observed RFI. Further on-site campaigns are expected in the future by refining the experimental setup with a complete decoupling of the GISTM/SDR acquisition chain (e.g., antenna) and by implementing a multifrequency acquisition unit (including L2/L5 GNSS bands). Moreover, by deploying multiple synchronous stations would allow to implement TDOA/FDOA interferer localization [66].

Acknowledgment

The authors would like to thank the National Agency for New Technologies, Energy, and Sustainable Economic Development (ENEA). The authors would also like to thank Alcide Giorgio di Sarra (scientific director of the activities at the ENEA Climate Observation Station) and Damiano Sferlazzo for providing us with the technical and logistical support during the measurements campaign and for the fruitful discussions.

References

[1] P. Kintner, B. Ledvina, and E. De Paula, "GPS and ionospheric scintillations," *Space Weather*, vol. 5, no. 9, 2007, Art. no. S09003.

[2] L. Spogli, L. Alfonsi, G. De Franceschi, V. Romano, M. H. O. Aquino, and A. Dodson, "Climatology of GPS ionospheric scintillations over high and mid-latitude European regions," *Annales Geophysicae*, vol. 27, no. 9, pp. 3429–3437, Sep. 2009, doi: 10.5194/angeo-27-3429-2009.

[3] R. S. Conker, M. B. El-Arini, C. J. Hegarty, and T. Hsiao, "Modeling the effects of ionospheric scintillation on GPS/Satellite-Based augmentation system availability," *Radio Sci.*, vol. 38, no. 1, Jan. 2003, Art. no. 1001, doi: 10.1029/2000RS002604.

[4] N. Balan, L. Liu, and H. Le, "A brief review of equatorial ionization anomaly and ionospheric irregularities," *Earth Planet. Phys.*, vol. 2, no. 4, pp. 257–275, 2018, doi: 10.26464/epp2018025.

[5] H. Ghobadi et al., "Disentangling ionospheric refraction and diffraction effects in GNSS raw phase through fast iterative filtering technique," *GPS Solutions*, vol. 24, no. 3, Jun. 2020, Art. no. 85, doi: 10.1007/s10291-020-01001-1.

[6] E. D. Kaplan and C. Hegarty, *Understanding GPS/GNSS: Principles and Applications*. Boston, MA, USA: Artech House, 2017.

[7] L. Alfonsi et al., "First observations of GNSS ionospheric scintillations from DemoGRAPE project," *Space Weather*, vol. 14, no. 10, pp. 704–709, 2016.

[8] J. Park, S. V. Veettil, M. Aquino, L. Yang, and C. Cesaroni, "Mitigation of ionospheric effects on GNSS positioning at low latitudes," *Navigation: J. Inst. Navigation*, vol. 64, no. 1, pp. 67–74, 2017.

[9] G. De Franceschi, L. Spogli, L. Alfonsi, V. Romano, C. Cesaroni, and I. Hunstad, "The ionospheric irregularities climatology over Svalbard from solar cycle 23," *Sci. Rep.*, vol. 9, no. 1, Jun. 2019, Art. no. 9232, doi: 10.1038/s41598-019-44829-5.

[10] C. Cesaroni et al., "L-band scintillations and calibrated total electron content gradients over Brazil during the last solar maximum," *J. Space Weather Space Climate*, vol. 5, 2015, Art. no. A36, doi: 10.1051/swsc/2015038.

[11] L. Spogli et al., "Formation of ionospheric irregularities over Southeast Asia during the 2015 St. Patrick's day storm," *J. Geophys. Res.: Space Phys.*, vol. 121, no. 12, pp. 12–211, Dec. 2016, doi: 10.1002/2016JA023222.

[12] O. Olwendo, C. Cesaroni, Y. Yamazaki, and P. Cilliers, "Equatorial ionospheric disturbances over the East African sector during the 2015 St. Patrick's Day storm," *Adv. Space Res.*, vol. 60, no. 8, pp. 1817–1826, Oct. 2017, doi: 10.1016/j.asr.2017.06.037.

[13] L. Spogli et al., "Ionospheric response over Brazil to the Aug. 2018 geomagnetic storm as probed by CSES-01 and swarm satellites and by local ground-based observations," *J. Geophys. Res.: Space Phys.*, vol. 126, no. 2, Feb. 2021, Art. no. e2020JA028368, doi: 10.1029/2020JA028368.

[14] L. Alfonsi et al., "Ionospheric disturbances over the Indian sector during 8 september 2017 geomagnetic storm: Plasma structuring and propagation," *Space Weather*, vol. 19, no. 3, Mar. 2021, Art. no. e2020SW002607, doi: 10.1029/2020SW002607.

[15] C. Cesaroni et al., "The first use of coordinated ionospheric radio and optical observations over Italy: Convergence of high-and low-latitude storm-induced effects," *J. Geophys. Res.: Space Phys.*, vol. 122, no. 11, pp. 11–794, Nov. 2017, doi: 10.1002/2017JA024325.

[16] E. Afraimovich, E. Astafyeva, V. Demyanov, and I. Gamayunov, "Mid-latitude amplitude scintillation of GPS signals and GPS performance slips," *Adv. Space Res.*, vol. 43, no. 6, pp. 964–972, 2009.

[17] S. Vadakke Veettil, H. Haralambous, and M. Aquino, "Observations of quiet-time moderate midlatitude L-band scintillation in association with plasma bubbles," *GPS Solutions*, vol. 21, no. 3, pp. 1113–1124, Jan. 2017, doi: 10.1007/s10291-016-0598-x.

[18] K. Kauristie et al., "Space weather services for civil aviation–challenges and solutions," *Remote Sens.*, vol. 13, no. 18, 2021, Art. no. 3685.

[19] G. De Franceschi, L. Alfonsi, and V. Romano, "ISACCO: An Italian project to monitor the high latitudes ionosphere by means of GPS receivers," *GPS Solutions*, vol. 10, no. 4, pp. 263–267, 2006.

[20] A. Van Dierendonck, J. Klobuchar, and Q. Hua, "Ionospheric scintillation monitoring using commercial single frequency C/A code receivers," in *Proc. ION GPS*, 1993, vol. 93, pp. 1333–1342.

[21] A. P. Cerruti, P. M. Kintner, D. E. Gary, L. J. Lanzerotti, E. R. de Paula, and H. B. Vo, "Observed solar radio burst effects on GPS/wide area augmentation system carrier-to-noise ratio," *Space Weather*, vol. 4, no. 10, 2006, Art. no. S10006. [Online]. Available: https://agupubs.onlinelibrary.wiley.com/doi/abs/10.1029/2006SW000254

[22] H. Sato et al., "Solar radio burst events on 6 Sep. 2017 and its impact on GNSS signal frequencies," *Space Weather*, vol. 17, no. 6, pp. 816–826, 2019. [Online]. Available: https://agupubs.onlinelibrary.wiley.com/doi/abs/10.1029/2019SW002198

[23] G. de Oliveira Nascimento Brassarote, E. M. de Souza, and J. F. G. Monico, "S4 index: Does it only measure ionospheric scintillation?," *GPS Solutions*, vol. 22, no. 1, 2018, Art. no. 8.

[24] G. D'Angelo, L. Spogli, C. Cesaroni, V. Sgrigna, L. Alfonsi, and M. Aquino, "GNSS data filtering optimization for ionospheric observation," *Adv. Space Res.*, vol. 56, no. 11, pp. 2552–2562, Dec. 2015, doi: 10.1016/j.asr.2015.10.002.

[25] R. Romero and F. Dovis, "Towards analyzing the effect of interference monitoring in GNSS scintillation," in *Mitigation of Ionospheric Threats to GNSS*, R. Notarpietro, F. Dovis, G. D. Franceschi, and M. Aquino, Eds. Rijeka, Croatia: IntechOpen, 2014, ch. 4. [Online]. Available: https://doi.org/10.5772/58768

[26] R. Romero and F. Dovis, "Effect of interference in the calculation of the amplitude scintillation index S4," in *Proc. Int. Conf. Localization GNSS*, 2013, pp. 1–6.

[27] Y. Liao and Y. Zou, "Impact of radio frequency interference on GNSS ionospheric scintillation data analysis," in *Proc. 13th Int. Symp. Antennas, Propag. EM Theory*, 2021, pp. 1–3.

[28] F. Dovis, *GNSS Interference Threats and Countermeasures*. Boston, MA, USA: Artech House, 2015.

[29] Z. Zhang, Y. Qu, Z. Wu, M. J. Nowak, J. Ellinger, and M. C. Wicks, "RF steganography via LFM chirp radar signals," *IEEE Trans. Aerosp. Electron. Syst.*, vol. 54, no. 3, pp. 1221–1236, Jun. 2018.

[30] Z. Zhang, M. J. Nowak, M. Wicks, and Z. Wu, "Bio-inspired RF steganography via linear chirp radar signals," *IEEE Commun. Mag.*, vol. 54, no. 6, pp. 82–86, Jun. 2016.

[31] B. Motella, S. Savasta, D. Margaria, and F. Dovis, "Method for assessing the interference impact on GNSS receivers," *IEEE Trans. Aerosp. Electron. Syst.*, vol. 47, no. 2, pp. 1416–1432, Apr. 2011.

[32] S. Peng and Y. Morton, "A USRP2-based reconfigurable multi-constellation multi-frequency GNSS software receiver front end," *GPS Solutions*, vol. 17, no. 1, pp. 89–102, 2013.

[33] G. Lachapelle and A. Broumandan, "Benefits of GNSS IF data recording," in *Proc. Eur. Navigation Conf.*, 2016, pp. 1–6.

[34] N. Linty, F. Dovis, and L. Alfonsi, "Software-defined radio technology for GNSS scintillation analysis: Bring antarctica to the lab," *GPS Solutions*, vol. 22, no. 4, pp. 1–12, 2018.

[35] N. Linty, F. Dovis, R. Romero, C. Cristodaro, L. Alfonsi, and E. Correia, "Monitoring ionosphere over Antarctica by means of a GNSS signal acquisition system and a software radio receiver," in *Proc. Int. Tech. Meeting Inst. Navigation*, 2016, pp. 549–555.

[36] C. Ruf, S. Gross, and S. Misra, "RFI detection and mitigation for microwave radiometry with an agile digital detector," *IEEE Trans. Geosci. Remote Sens.*, vol. 44, no. 3, pp. 694–706, Mar. 2006.

[37] J. R. Piepmeier et al., "Radio-frequency interference mitigation for the soil moisture active passive microwave radiometer," *IEEE Trans. Geosci. Remote Sens.*, vol. 52, no. 1, pp. 761–775, Jan. 2014.

[38] P. N. Mohammed, M. Aksoy, J. R. Piepmeier, J. T. Johnson, and A. Bringer, "SMAP L-band microwave radiometer: RFI mitigation prelaunch analysis and first year on-orbit observations," *IEEE Trans. Geosci. Remote Sens.*, vol. 54, no. 10, pp. 6035–6047, Oct. 2016.

[39] F. Ticconi, C. Anderson, J. Figa-Saldaña, J. J. W. Wilson, and H. Bauch, "Analysis of radio frequency interference in metop ASCAT backscatter measurements," *IEEE J. Sel. Topics Appl. Earth Observ. Remote Sens.*, vol. 10, no. 5, pp. 2360–2371, May 2017.

[40] E. Pica et al., "The SWIT-eSWua system: Managing, preservation and sharing of the historical and near real-time ionospheric data at the INGV," in *Proc. Amer. Geophys. Union Fall Meeting*, Mar. 2021, doi: 10.1002/essoar.10506618.1.

[41] G. Garelli and M. Tazzioli, "The EU hotspot approach at Lampedusa," *Open Democracy*, 2016. [Online]. Available: https://www.opendemocracy.net/en/can-europe-make-it/eu-hotspot-approach-at-lampedusa/

[42] E. Pulitano, *Island(s): Lampedusa as a "Hotspot" of EU Border Policies*. Cham, Switzerland: Springer, 2022, pp. 43–73, doi: 10.1007/978-3-031-05992-6_3.

[43] A. I. U. Eurocontrol, "Does radio frequency interference to satellite navigation pose an increasing threat to network efficiency, cost-effectiveness and ultimately safety?," Eurocontrol, Brussels, Belgium, Think Paper, 2021.

[44] T. M. Roberts, T. K. Meehan, J. Y. Tien, and L. E. Young, "Detection and localization of terrestrial L-band RFI with GNSS receivers," *IEEE Trans. Geosci. Remote Sens.*, vol. 60, Sep. 2021, Art. no. 5801311, doi: 10.1109/TGRS.2021.3109524.

[45] N. Linty, A. Minetto, F. Dovis, and L. Spogli, "Effects of phase scintillation on the GNSS positioning error during the september 2017 storm at Svalbard," *Space Weather*, vol. 16, no. 9, pp. 1317–1329, 2018.

[46] C. Cristodaro, F. Dovis, N. Linty, and R. Romero, "Design of a configurable monitoring station for scintillations by means of a GNSS software radio receiver," *IEEE Geosci. Remote Sens. Lett.*, vol. 15, no. 3, pp. 325–329, Mar. 2018.

[47] P. Misra and P. Enge, *Global positioning system: Signals, Measurements, and Performance*, 2nd ed. Nanded, India: Ganga-Jamuna Press, 2006.
[48] M. Pini, E. Falletti, and M. Fantino, "Performance evaluation of C/N0 estimators using a real time GNSS software receiver," in *Proc. IEEE 10th Int. Symp. Spread Spectr. Techn. Appl.*, 2008, pp. 32–36.
[49] L. Alfonsi et al., "Bipolar climatology of GPS ionospheric scintillation at solar minimum," *Radio Sci.*, vol. 46, no. 3, 2011, Art. no. RS0D05.
[50] C. Cesaroni et al., "Electronic space weather upper atmosphere database (eSWua) - GNSS scintillation data, version 1.0," Nat. Inst. Geophys. Volcanology, Rome, Italy, 2020.
[51] F. S. Rodrigues, J. G. Socola, A. O. Moraes, C. Martinis, and D. A. Hickey, "On the properties of and ionospheric conditions associated with a mid-latitude scintillation event observed over southern United States," *Space Weather*, vol. 19, no. 6, Jun. 2021, Art. no. e2021SW002744, doi: 10.1029/2021SW002744.
[52] B. M. Ledvina, J. J. Makela, and P. M. Kintner, "First observations of intense GPS L1 amplitude scintillations at midlatitude," *Geophys. Res. Lett.*, vol. 29, no. 14, pp. 4-1–4-4, Jul. 2002, doi: 10.1029/2002GL014770.
[53] N. Balan, K. Shiokawa, Y. Otsuka, S. Watanabe, and G. J. Bailey, "Super plasma fountain and equatorial ionization anomaly during penetration electric field," *J. Geophys. Res. Space Phys.*, vol. 114, no. A3, Mar. 2009, Art. no. A03310, doi: 10.1029/2008JA013768.
[54] D. Di Mauro et al., "Geomagnetic activity at Lampedusa island: Characterization and comparison with the other Italian observatories, also in response to space weather events," *Remote Sens.*, vol. 13, no. 16, Aug. 2021, Art. no. 3111, doi: 10.3390/rs13163111.
[55] P. Bagiacchi, G. Benedetti, L. Cafarella, D. Di Mauro, and A. E. Zirizzotti, "The new system for data acquisition and visualisation of the magnetic field of the Earth," *Rapporti Tecnici INGV*, vol. 428, Feb. 2021. [Online]. Available: http://editoria.rm.ingv.it/rapporti/2021/rapporto428/
[56] J. Uwamahoro and J. Habarulema, "Empirical modeling of the storm time geomagnetic indices: A comparison between the local K and global KP indices," *Earth, Planets Space*, vol. 66, no. 1, 2014, Art. no. 95, doi: 10.1186/1880-5981-66-95.
[57] L. Spogli et al., "Adaptive phase detrending for GNSS scintillation detection: A case study over Antarctica," *IEEE Geosci. Remote Sens. Lett.*, vol. 19, Apr. 2021, Art no. 8009905, doi: 10.1109/LGRS.2021.3067727.
[58] P. Welch, "The use of fast fourier transform for the estimation of power spectra: A method based on time averaging over short, modified periodograms," *IEEE Trans. Audio Electroacoust.*, vol. 15, no. 2, pp. 70–73, Jun. 1967.
[59] M. H. Hayes, *Statistical Digital Signal Processing and Modeling*. Hoboken, NJ, USA: Wiley, 2009.
[60] F. J. Harris, "On the use of windows for harmonic analysis with the discrete Fourier transform," *Proc. IEEE*, vol. 66, no. 1, pp. 51–83, Jan. 1978.
[61] L. Cohen, *Time-Frequency Analysis*. Englewood Cliffs, NJ, USA: Prentice Hall, 1995, vol. 778.
[62] M. Kronauge and H. Rohling, "New chirp sequence radar waveform," *IEEE Trans. Aerosp. Electron. Syst.*, vol. 50, no. 4, pp. 2870–2877, Oct. 2014.
[63] D. Borio and C. Gioia, "Mitigation of frequency-hopped tick jamming signals," in *Proc. IEEE/ION Position, Location Navigation Symp.*, 2020, pp. 624–630.
[64] F. C. Commission, "Enforcement advisory: Warning: Jammer use is prohibited; prohibition applies to use by the public and state and local government agencies," Federal Commun. Commission, Washington, DC, USA, Public Notice/Advisory DA-14-1785, 2014.
[65] M. J. Murrian et al., "First results from three years of GNSS interference monitoring from low earth orbit," *Navigation*, vol. 68, no. 4, pp. 673–685, 2021.
[66] N. O'Donoughue, *Emitter Detection and Geolocation for Electronic Warfare*. Norwood, MA, USA: Artech House, 2019.
[67] K. Becker, "An efficient method of passive emitter location," *IEEE Trans. Aerosp. Electron. Syst.*, vol. 28, no. 4, pp. 1091–1104, Oct. 1992.
[68] A. G. Dempster and E. Cetin, "Interference localization for satellite navigation systems," *Proc. IEEE*, vol. 104, no. 6, pp. 1318–1326, Jun. 2016.

Emanuele Pica received the B.Sc. degree in electronic engineering from the University of Salerno, Salerno, Italy, in 2013, and the M.Sc. degree in space and astronautical engineering from Sapienza University, Rome, Italy, in 2018.

He is currently a Technologist with Istituto Nazionale di Geofisica e Vulcanologia (INGV), Rome, Italy. He is currently responsible for the INGV ionospheric scintillations network. His research interests include research data management, research infrastructures, and ionospheric monitoring.

Alex Minetto (Member, IEEE) was born in Pinerolo, Italy, in 1990. He received the B.Sc. degree in communications engineering, the M.Sc. degree in telecommunications engineering, and the Ph.D. degree in electrical, electronics, and communications engineering from Politecnico di Torino, Turin, Italy, in 2015, 2016, and 2020, respectively.

He joined the Department of Electronics and Telecommunications, Politecnico di Torino, in 2022 as a Researcher and Assistant Professor. His current research interests cover navigation signal design and processing, advanced Bayesian estimation applied to positioning and navigation technologies (PNT), and applied Global Navigation Satellite System (GNSS) applied to space weather and space positioning, navigation, and timing technologies.

Claudio Cesaroni received the M.Sc. degree in physics from Sapienza University of Rome, Rome, Italy, in 2011, and the Ph.D. degree in geophysics from Alma Mater Studiorum University of Bologna, Bologna, Italy, in 2015.

He is currently a Researcher with Istituto Nazionale di Geofisica e Vulcanologia, Rome, Italy, and responsible of the Upper Atmosphere Physics and Radiopropagation Unit. He is an Expert in ionospheric physics, in data analysis and treatment techniques focused on TEC calibration technique and effects of spatial and temporal gradients on GNSS signals. He developed algorithms for the analysis of TEC gradients and scintillations data at low latitudes and for the analysis of the dynamics of the ionospheric irregularities. He was also involved in the IPS project and in the PECASUS consortium for the development of models and tools to nowcast and forecasting TEC gradients effects on GNSS signals. He took part to several Antarctic and Arctic scientific expeditions. He is the author of an international patent: Grzesiak M, Cesaroni, C., Spogli, L., De Franceschi, G. "Method for forecasting ionosphere total electron content and/or scintillation parameters", International Publication Number WO 2016/185500 A1.

Fabio Dovis (Member, IEEE) was born in Bruino, Italy, in 1970. He received the M.Sc. and Ph.D. degrees in electronics engineering from Politecnico di Torino, Turin, Italy, in 1996 and 2000, respectively.

He joined the Department of Electronics and Telecommunications, Politecnico di Torino, an Assistant Professor in 2004 and as Associate Professor in 2014. Since 2021, he has been a Full Professor with the Department of Electronics and Telecommunications where he coordinates the Navigation Signal Analysis and Simulation (NavSAS) research group. He has a relevant experience in European projects in satellite navigation as well as cooperation with industries and research institutions. His research interests include the design of GPS and Galileo receivers, advanced signal processing for interference and multipath detection and mitigation, and ionospheric monitoring.

Dr. Dovis is a Member of the IEEE Aerospace and Electronics Systems Society Navigation Systems Panel.